Davide Pini <sup>(1)</sup>; Santi Prestipino <sup>(1)</sup>; Dino Costa <sup>(1)</sup>; Gianpietro Malescio; Gianmarco Munaò <sup>(2)</sup>



J. Chem. Phys. 163, 164905 (2025) https://doi.org/10.1063/5.0291013





## **Articles You May Be Interested In**

Liquid—liquid equilibria for soft-repulsive particles: Improved equation of state and methodology for representing molecules of different sizes and chemistry in dissipative particle dynamics

J. Chem. Phys. (January 2015)

Thermally activated intermixture in pentacene-perfluoropentacene heterostructures

J. Chem. Phys. (March 2013)

Two-dimensional mixture of amphiphilic dimers and spheres: Self-assembly behaviour

J. Chem. Phys. (October 2017)



# A density-functional theory study of vapor, liquid, and mesophases in a symmetric, hard-sphere mixture with cross attraction at non-equimolar concentrations

Cite as: J. Chem. Phys. 163, 164905 (2025); doi: 10.1063/5.0291013 Submitted: 15 July 2025 • Accepted: 30 September 2025 •







**Published Online: 23 October 2025** 









## **AFFILIATIONS**

- Dipartimento di Fisica "A. Pontremoli," Università degli Studi di Milano, Via Celoria 16, 20133 Milano, Italy
- <sup>2</sup>Dipartimento di Scienze Matematiche e Informatiche, Scienze Fisiche e Scienze della Terra, Università degli Studi di Messina, Viale F. Stagno d'Alcontres 31, 98166 Messina, Italy

#### **ABSTRACT**

We investigate the phase diagram of a model hard-sphere mixture consisting of two species of equal diameter, featuring a square-well cross attraction. The study is carried out using density-functional theory (DFT) in the mean-field approximation and extends to arbitrary species concentrations a former DFT study at equimolar composition [Prestipino et al., J. Chem. Phys. 159, 204902 (2023)]. In addition to the stripe phases found in the equimolar case, cylinder and cluster phases are also observed. While at high temperatures, the inhomogeneous domains can be accessed only from the high-density liquid; at low temperatures, these phases coexist with the low-density vapor, resulting in a notably rich phase diagram. The predictions of an analytic implementation of the theory—based on the Landau expansion of the free energy in powers of the density modulation amplitude—are compared with numerical DFT minimization. The Landau approach shows qualitative agreement, although it overestimates the extent of the stripe region at high density, where local concentration values may exceed their physical bounds. Differences and similarities between DFT and simulation results for narrow attractive wells are briefly discussed.

Published under an exclusive license by AIP Publishing, https://doi.org/10.1063/5.0291013

## I. INTRODUCTION

The appearance of complex supramolecular aggregates originated by the self-assembly of simpler building blocks is a distinctive feature of soft matter. 1,2 In this field, computationally based approaches are largely implemented to model such building blocks toward a desired structure.<sup>3,4</sup> Mesophases, like, for instance, lamellar, cylindrical, gyroidal, or cluster phases, 5,6 spontaneously arise in a large variety of soft-matter systems, including block copolymers, colloids, 9,10 and amphiphilic systems. 11,1

These non-trivial structures may occur even in the presence of purely spherically symmetric forces between their components. A simple instance is represented by hard-core particles that feature a short-range attraction and a longer-range repulsion (SALR). 13-16 In SALR fluids, by properly tuning the repulsion range, it is possible to

"switch" from a simple liquid to a cluster fluid 17-20 which, for sufficiently strong repulsion, at low temperature arranges into periodic structures, superseding the usual vapor-liquid phase separation.

Another example consists of the so-called core-corona interactions, where a hard-core repulsion is followed by a square-well shoulder or a similar bounded repulsion at a larger distance. <sup>21–27</sup> In this case, mesophases are favored by the fact that the energy that two particles have to pay to come close to each other is independent of the degree of overlap of their soft repulsive shells, or nearly so. Therefore, particles may find it energetically convenient to form dense, separate aggregates in such a way that the repulsive interaction between particles belonging to distinct aggregates is weak or

Spontaneous pattern formation is observed not only in monodisperse systems but also in binary mixtures in which the

a) Author to whom correspondence should be addressed: gianmarco.munao@unime.it

potential between particles of the same species is again of SALR<sup>28-32</sup> or core-corona type, <sup>33,34</sup> whereas the sign of the potential is reversed for particles of different species. In the cross interaction, the SALR and the repulsive corona are then replaced, respectively, by a short-range repulsion followed by a longer-range attraction and by an attractive well.

Interestingly, even interactions that, in pure fluids, do not form mesophases may do so when one moves to mixtures. One such instance, which we have recently investigated, 35,36 concerns the occurrence of stripe patterns in a binary mixture of hard spheres of the same size at equal concentration, mutually interacting through a square-well attraction. Stripes have been observed in a large variety of different systems, including photonic crystals,<sup>37</sup> amphiphilic surfaces,<sup>38</sup> and colloidal particles,<sup>39</sup> as well as in living matter.<sup>40,41</sup> In Ref. 36, stripes consist of periodic modulations of the local densities of both species along a given direction, in such a way that the total density remains nearly uniform, and the modulations affect the local concentration mostly. While in core-corona fluids, the vapor-liquid transition never occurs, and in SALR fluids, vapor-liquid phase separation and mesophase formation are mutually exclusive; this model mixture, instead, displays both transitions so that stripes can be accessed from both the liquid and the vapor phases.

The purpose of the present study is to generalize our former investigation<sup>36</sup> to concentrations other than equimolar. To this end, we employ the same mean-field density-functional theory (DFT) already implemented there. DFT-based approaches have been extensively adopted in the literature to describe mesophases, including cylindrical and lamellar structures, as well as clusters and percolated phases. <sup>6,17,19,42–44</sup>

When moving away from equimolarity, in addition to the stripe phases, we now predict the existence of doubly and triply periodic mesophases, whereby the less abundant species arrange into periodic arrays of aggregates with cylindrical or spherical shapes, and the more abundant species fills the region left available. As in the equimolar case, both liquid-mesophase and vapor-mesophase transitions are possible, resulting in a considerably rich phase diagram.

The present paper follows a recent investigation of the same system based on numerical simulation, <sup>45</sup> aimed at the characterization of the crystal structures for narrow attractive wells. Since the DFT used here is not suited to tackle this problem, the two studies should be regarded as complementary; although an attempt to compare some of their predictions is presented below.

This study is organized as follows: in Sec. II, details concerning the model potential and the calculation of spinodal and  $\lambda$ -surfaces are provided. Critical lines are discussed in Sec. III, while the equations describing vapor–liquid phase equilibrium are presented in Sec. IV. In Sec. V, an analytic treatment of the inhomogeneous phases based on the Landau expansion of the free energy is described. The phase diagram is addressed in Sec. VI: in Sec. VI A, the outcome of the Landau theory is discussed, while in Sec. VI B, it is compared to the predictions of the numerical minimization of the free-energy functional. The comparison with the aforementioned simulation study of the same mixture<sup>45</sup> is addressed in Sec. VI C. Finally, in Sec. VII, we present our conclusions and perspectives. The detailed derivation of the results of the Landau theory presented in Sec. V is reported in the Appendix.

#### II. SPINODAL AND $\lambda$ -SURFACES

We consider the same hard-sphere mixture of two species 1 and 2 investigated at equimolar concentration in Refs. 35 and 36. The two species have the same diameter  $\sigma$ , and the off-core part of the interaction  $w_{ij}(r)$  between particles of the same species vanishes, whereas for particles of different species it consists of a square-well attraction of depth  $\varepsilon$  and range  $\xi = (1 + y)\sigma$ , where  $\xi$  is measured from r = 0, and  $\gamma$  is the well width in units of  $\sigma$ . We then have  $w_{11}(r) = w_{22}(r) \equiv 0$  and

$$w_{12}(r) = w_{21}(r) \equiv w(r) = \begin{cases} -\varepsilon, & r \le \xi, \\ 0, & r > \xi. \end{cases}$$
 (1)

In the following, we shall denote by  $\rho_i$  the average density  $N_i/V$  of species i—where  $N_i$  is the number of particles of species i and V is the volume—and by  $\rho_i(\mathbf{r})$  the local density of species i at  $\mathbf{r}$ . We also introduce the total density  $\rho = \rho_1 + \rho_2$ , the concentration  $x = \rho_2/\rho$ , and the rescaled concentration y = 1 - 2x. Clearly, one has  $0 \le x \le 1$  and  $-1 \le y \le 1$ , the equimolar concentration corresponding to y = 0.

The present investigation is based on the same mean-field Helmholtz free-energy functional already adopted in the equimolar case, <sup>36</sup>

$$\beta A[\rho_{1}(\mathbf{r}), \rho_{2}(\mathbf{r})] = \int d^{3}\mathbf{r} \frac{\beta A_{\text{ID}}^{\text{mix}}}{V} (\rho_{1}(\mathbf{r}), \rho_{2}(\mathbf{r}))$$

$$+ \int d^{3}\mathbf{r} \frac{\beta A_{\text{HS}}^{\text{ex, mix}}}{V} (\rho_{1}(\mathbf{r}), \rho_{2}(\mathbf{r}))$$

$$+ \frac{\beta}{2} \sum_{i,j=1}^{2} \int d^{3}\mathbf{r} \int d^{3}\mathbf{r}' w_{ij}(\mathbf{r} - \mathbf{r}') \rho_{i}(\mathbf{r}) \rho_{j}(\mathbf{r}'), \quad (2)$$

where  $\beta = 1/(k_B T)$  is the inverse temperature,  $A_{\rm ID}^{\rm mix}$  is the Helmholtz free energy of a binary mixture of ideal gases given by

$$\frac{\beta A_{\text{ID}}^{\text{mix}}}{V} = \sum_{i=1}^{2} \rho_i \left[ \ln \left( \rho_i \Lambda^3 \right) - 1 \right], \tag{3}$$

A being the thermal wavelength, and  $A_{\rm HS}^{\rm ex,\,mix}$  is the excess Helmholtz free energy of a binary mixture of hard spheres. While the ideal-gas term of Eq. (3) is, of course exact, the hard-sphere contribution is taken into account in the local density approximation (LDA). In the present case, in which the two species have the same diameter, one has

$$A_{\mathrm{HS}}^{\mathrm{ex,\,mix}}(\rho_1(\mathbf{r}),\rho_2(\mathbf{r})) = A_{\mathrm{HS}}^{\mathrm{ex}}(\rho_1(\mathbf{r}) + \rho_2(\mathbf{r})), \tag{4}$$

where  $A_{\rm HS}^{\rm ex}$  is the excess Helmholtz free energy of a one-component hard-sphere fluid, for which we have adopted the Carnahan–Starling expression

$$\frac{\beta A_{\rm HS}^{\rm ex}}{V} = \frac{\eta^2 (4 - 3\eta)}{v_0 (1 - \eta)^2},\tag{5}$$

where  $\eta = \rho v_0$  is the total packing fraction and  $v_0 = \pi \sigma^3/6$  is the hard-sphere volume.

The condition of stability of the homogeneous phase  $\rho_i(\mathbf{r}) \equiv \rho_i$  against small density perturbations  $\delta \rho_i(\mathbf{r})$ , i = 1, 2, reads

$$\sum_{i,i=1}^{2} \int d^{3}\mathbf{r} \int d^{3}\mathbf{r}' C_{ij}(\mathbf{r} - \mathbf{r}') \delta \rho_{i}(\mathbf{r}) \delta \rho_{j}(\mathbf{r}') < 0, \tag{6}$$

where  $C_{ij}(\mathbf{r} - \mathbf{r}')$  is the direct correlation function of the homogeneous fluid,

$$C_{ij}(\mathbf{r} - \mathbf{r}') \equiv \left. \frac{\delta^2(-\beta A)}{\delta \rho_i(\mathbf{r}) \delta \rho_j(\mathbf{r}')} \right|_{\rho_i, \rho_i}.$$
 (7)

We remark that here, at variance with the more widely adopted definition, the direct correlation function  $C_{ij}(r)$  includes the ideal-gas contribution and, therefore, is related to the usual Ornstein–Zernike direct correlation function  $c_{ij}(r)$  by

$$C_{ij}(r) = -\delta(r)\frac{\delta_{ij}}{\rho_i} + c_{ij}(r), \tag{8}$$

or

$$\widetilde{C}_{ij}(k) = -\frac{\delta_{ij}}{\rho_i} + \widetilde{c}_{ij}(k), \tag{9}$$

where  $\delta(r)$  is the Dirac delta,  $\delta_{ij}$  is the Kronecker delta, r is the modulus of  $\mathbf{r}$ , k is the modulus of the wave vector  $\mathbf{k}$ , and the tilde denotes the Fourier transform,

$$\widetilde{c}_{ij}(k) = \int d^3 \mathbf{r} e^{-i\mathbf{k}\cdot\mathbf{r}} c_{ij}(r). \tag{10}$$

Equation (6) is equivalent to requiring that the matrix  $\|\widetilde{C}_{ij}(k)\|$  be negative definite for every k. By substituting Eq. (2) into Eq. (7), we obtain

$$\widetilde{C}_{ij}(k) = -\frac{\delta_{ij}}{\rho_i} + \widetilde{c}_{ij}^{HS}(0) - \beta \widetilde{w}_{ij}(k), \tag{11}$$

where  $\widetilde{c}_{ij}^{HS}(0)$  is the Fourier transform of the Ornstein–Zernike direct correlation function of the hard-sphere mixture at k=0. For the system at hand, for which the two species have the same diameter  $\sigma$ ,  $c_{ij}^{HS}(r)$  is actually independent of the indices i,j and coincides with the direct correlation function  $c_{HS}(r)$  of a one-component hard-sphere fluid of diameter  $\sigma$  at density  $\rho$ , equal to the total density of the mixture. According to Eq. (5), one has

$$\widetilde{c}_{\text{HS}}(0) = -\frac{d^2}{d\rho^2} \left( \frac{\beta A_{\text{HS}}^{\text{ex}}}{V} \right) = -2v_0 \frac{4-\eta}{(1-\eta)^4}.$$
 (12)

Hereafter, we shall set  $c_0 \equiv \widetilde{c}_{HS}(0)$ . We then obtain from Eq. (11),

$$\|\widetilde{C}_{ij}(k)\| = \begin{pmatrix} -\frac{1}{\rho_1} + c_0 & c_0 - \beta \widetilde{w}(k) \\ c_0 - \beta \widetilde{w}(k) & -\frac{1}{\rho_2} + c_0 \end{pmatrix},$$
(13)

where the Fourier transform  $\widetilde{w}(k)$  of the square-well potential is given by

$$\widetilde{w}(k) = -\frac{4\pi\varepsilon}{k^3} [\sin(k\xi) - k\xi \cos(k\xi)]. \tag{14}$$

The quantity  $\widetilde{C}_{11}$  is always negative, so  $\|\widetilde{C}_{ij}(k)\|$  is negative definite if and only if its determinant det  $\|\widetilde{C}_{ij}(k)\|$  is positive for every k. Since  $\widetilde{C}_{22}$  is also negative, the product  $\widetilde{C}_{11}\widetilde{C}_{22}$  is positive, and we may set

$$B^{2} = \left(-\frac{1}{\rho_{1}} + c_{0}\right) \left(-\frac{1}{\rho_{2}} + c_{0}\right),\tag{15}$$

which gives

$$\det \|\widetilde{C}_{ij}(k)\| = [B - c_0 + \beta \widetilde{w}(k)] B + c_0 - \beta \widetilde{w}(k)].$$
 (16)

Let us consider the first factor in the rhs of Eq. (16) at k=0. Since  $B-c_0$  is positive at all densities and concentrations and  $\widetilde{w}(0)$  is negative, this factor changes sign from positive to negative as  $\beta$  is increased. Moreover, since  $\widetilde{w}(k)$  takes its absolute minimum at k=0, the first wave vector at which the sign of the first factor changes is indeed k=0, leading to an instability at  $\beta_0=B-c_0$ , where we have introduced the quantity  $\beta_0\equiv\beta|\widetilde{w}(0)|$ . This is the spinodal instability, whereby the homogeneous fluid becomes unstable by developing long-wavelength fluctuations that give rise to vapor–liquid phase separation. By solving the equation  $\beta_0=B-c_0$  with respect to the concentration, we find the expression of the rescaled concentration along the spinodal surface  $y_*(\rho,\beta)$ ,

$$y_{s} = \pm \sqrt{1 - \frac{4(1 - \rho c_{0})}{\rho^{2} \beta_{0}(\beta_{0} + 2c_{0})}}.$$
 (17)

The condition that the expression under the radical be non-negative requires

$$\beta_0 \ge \frac{2}{\rho} (1 - \rho c_0) = \frac{2}{\rho} + \frac{4v_0(4 - \eta)}{(1 - \eta)^4},$$
 (18)

where the equality holds at y = 0 and yields the spinodal curve in the temperature-density plane at equimolar concentration. Hence, at fixed density, the highest temperature on the spinodal is always obtained at equimolar concentration.

We now turn to the second factor in the rhs of Eq. (16). Since  $B+c_0$  is always positive, in order for this factor to turn from positive to negative, it must be evaluated at a wave vector k such that  $\widetilde{w}(k)$  is positive. Specifically, the first wave vector at which the second factor changes sign as  $\beta$  is increased is the k at which  $\widetilde{w}(k)$  assumes its (positive) maximum. For the square-well potential at hand, the maximum is located at  $k_0\xi \simeq 5.763$ . We are then in the presence of a Kirkwood instability  $^{46}$  at  $k_0 \neq 0$ , whereby the homogeneous fluid becomes unstable because of the onset of inhomogeneities modulated with a wavelength of  $\sim 2\pi/k_0$ . The boundary of the domain of instability, dubbed the  $\lambda$ -surface, corresponds to  $\beta_\lambda = B + c_0$ , where we have set  $\beta_\lambda = \beta \widetilde{w}(k_0)$ . The rescaled concentration on the  $\lambda$ -surface  $y_\lambda(\rho,\beta)$  is then

$$y_{\lambda} = \pm \sqrt{1 - \frac{4(1 - \rho c_0)}{\rho^2 \beta_{\lambda}(\beta_{\lambda} - 2c_0)}}.$$
 (19)

The condition that the expression under the radical be non-negative gives

$$\beta_{\lambda} \ge \frac{2}{\rho},$$
 (20)

where the equality describes the  $\lambda$ -line in the temperature-density plane at equimolar concentration. Therefore, at fixed density the equimolar concentration corresponds to the highest temperature not only along the spinodal but along the  $\lambda$ -line as well.

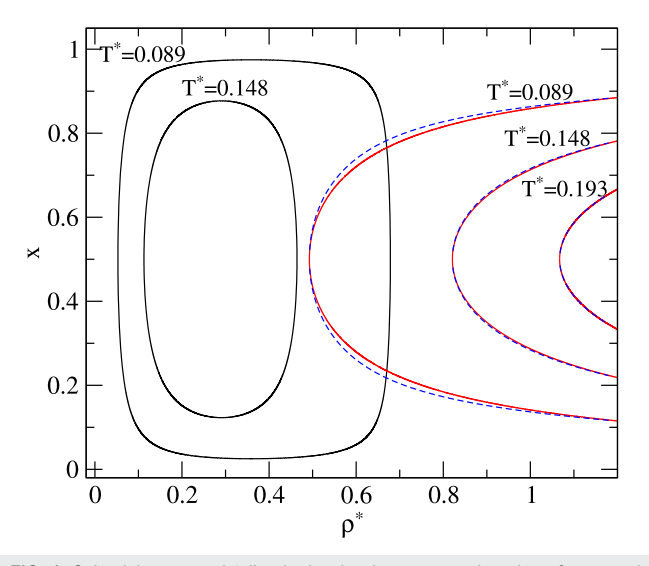
We remark that the above-mentioned analysis of the instabilities of the homogeneous phase was already carried out in Ref. 47, the mixture in hand corresponding to case III of Sec. 4.2 therein, although the detailed study of the phase diagram was not pursued there.

Figure 1 displays the curves obtained by taking a section of the spinodal and  $\lambda$ -surfaces in the density-concentration plane for three different temperatures. From now on, temperature and density will be measured in reduced units such that  $\beta^* = \beta \varepsilon (1 + \gamma)^3$ ,  $T^* = 1/\beta^*$ , and  $\rho^* = \rho \sigma^3$ . We remark that, since in Eqs. (17) and (19) the well width  $\gamma$  is contained only in the quantities  $\beta_0$ ,  $\beta_\lambda$  introduced earlier, the dependence of the spinodal and  $\lambda$ -surfaces on  $\gamma$  is entirely accounted for in the definition of  $T^*$ .

At relatively high temperature, the spinodal (black lines) is absent, and only the  $\lambda$ -line (in red) appears at high density. At lower temperatures, both the spinodal and the  $\lambda$ -line are present, and the domains bounded by the two curves are disconnected. As the temperature is further lowered, both domains grow in size and partially overlap. On this basis, we can expect different kinds of phase equilibria on changing the temperature, as will be discussed in Sec. VI.

We observe that, at variance with the equimolar case, the abovementioned results are not strictly equivalent to those that would be obtained by describing the direct correlation function  $C_{ij}(r)$  by the random phase approximation (RPA). In the RPA, one has

$$\widetilde{C}_{ij}(k) = -\frac{\delta_{ij}}{\rho_i} + \widetilde{c}_{ij}^{HS}(k) - \beta \widetilde{w}_{ij}(k), \qquad (21)$$



**FIG. 1.** Spinodal curve and  $\lambda$ -line in the density-concentration plane for several reduced temperatures  $T^* = k_{\rm B}T/[\varepsilon(1+\gamma)^3]$  displayed in the figure, corresponding to  $\gamma=0.5$  and  $k_{\rm B}T/\varepsilon=0.65, 0.5, 0.3$ . Black lines: spinodal curves. Red lines: LDA  $\lambda$ -lines. Blue lines: RPA  $\lambda$ -lines (see text). At  $T^*=0.193$ , the spinodal curve is absent.

which differs from LDA Eq. (11) inasmuch as the dependence of the direct correlation function of the hard-sphere fluid on the wave vector k is explicitly taken into account, whereas in the LDA this dependence is disregarded by having  $\widetilde{c}_{\rm HS}(k) \equiv c_0$ . As a consequence, according to the RPA, in Eqs. (15) and (16), the quantity  $c_0$  should be replaced by  $\widetilde{c}_{\rm HS}(k)$ . Since the spinodal instability does occur at k=0, the spinodal surface remains unchanged, but this does not apply to the  $\lambda$ -surface. If we denote by  $\widetilde{B}^2(k)$  the quantity obtained by replacing  $c_0$  with  $\widetilde{c}_{\rm HS}(k)$  in Eq. (15), the  $\lambda$ -surface is now identified by the equations

$$\widetilde{B}(k) + \widetilde{c}_{HS}(k) - \beta \widetilde{w}(k) = 0,$$
 (22a)

$$\frac{\partial}{\partial k} \left[ \widetilde{B}(k) + \widetilde{c}_{HS}(k) - \beta \widetilde{w}(k) \right] = 0 \qquad k \neq 0,$$
 (22b)

where, at variance with the LDA, the wave vector that satisfies Eq. (22b) is state-dependent and no longer coincides with  $k_0$ . However, the deviations from  $k_0$  are rather small, and the RPA  $\lambda$ -surface does not differ much from the LDA one. In Fig. 1, the RPA  $\lambda$ -line (blue), obtained from Eq. (22) with the Verlet-Weis representation<sup>48</sup> for  $\widetilde{c}_{HS}(k)$ , is compared to the LDA  $\lambda$ -line (red). The differences are more marked at low temperature, with the RPA curve being slightly wider than the LDA one. As the temperature is raised, the two curves become virtually indistinguishable from each other. Irrespective of the temperature, at equimolar concentration, the  $\lambda$ -line does not contain  $\widetilde{c}_{HS}(k)$ ; see Eq. (20), so the LDA and RPA curves coincide. At any rate, in the following, we shall always consider the LDA  $\lambda$ -surface, consistent with the adoption of the free-energy functional (2).

## III. CRITICAL LINES

On the spinodal and  $\lambda$ -surfaces, the determinant of the matrix  $\|\widetilde{C}_{ij}(k)\|$  vanishes at k=0 and  $k=k_0$ , respectively. Hence, one of its eigenvalues must vanish. Since  $\|\widetilde{C}_{ij}(k)\|$  is symmetrical, it is diagonalized by a rotation, and its eigenvalues  $\lambda_+, \lambda_-$  are given by

$$\lambda_{\pm} = \frac{1}{2} \left( \widetilde{C}_{11} + \widetilde{C}_{22} \right) \pm \frac{1}{2} \sqrt{\left( \widetilde{C}_{11} - \widetilde{C}_{22} \right)^2 + 4 \widetilde{C}_{12}^2}, \tag{23}$$

where the plus sign corresponds to  $\lambda_+$  and the minus sign to  $\lambda_-$ , and it is understood that  $\widetilde{C}_{ij}(k)$  is evaluated at k=0 on the spinodal and at  $k=k_0$  on the  $\lambda$ -surface. Since  $\widetilde{C}_{11}$  and  $\widetilde{C}_{22}$  are both negative, the vanishing eigenvalue is  $\lambda_+$  in both cases, with  $\widetilde{C}_{12} = \left[\widetilde{C}_{11}\widetilde{C}_{22}\right]^{1/2}$  on the spinodal and  $\widetilde{C}_{12} = -\left[\widetilde{C}_{11}\widetilde{C}_{22}\right]^{1/2}$  on the  $\lambda$ -surface. From Eqs. (13) and (23), we find for k=0

$$\lambda_{\pm} = -\frac{1}{2} \left( \frac{1}{\rho_1} + \frac{1}{\rho_2} \right) + c_0 \pm \frac{1}{2} \sqrt{\left( \frac{1}{\rho_1} - \frac{1}{\rho_2} \right)^2 + 4(c_0 + \beta_0)^2}, \quad (24)$$

and the same expression with  $\beta_0$  replaced by  $-\beta_{\lambda}$  for  $k = k_0$ .

The eigenvectors  $\mathbf{u}_+$  and  $\mathbf{u}_-$ , corresponding, respectively, to  $\lambda_+$  and  $\lambda_-$ , identify two orthogonal axes. A point in the  $\rho_1$ – $\rho_2$  plane can be expressed in terms of its coordinates  $\psi_+$  and  $\psi_-$  along these axes as  $^{49}$ 

$$\rho_1 = \cos\theta \, \psi_+ - \sin\theta \, \psi_-, \tag{25a}$$

$$\rho_2 = \sin\theta \, \psi_+ + \cos\theta \, \psi_-, \tag{25b}$$

where  $\vartheta$  is the angle of the rotation that casts  $\|\widetilde{C}_{ij}(k)\|$  into diagonal form. One has

$$\cos\theta = \sqrt{\frac{1}{2} + \frac{y}{\Delta}},\tag{26a}$$

$$\sin\theta = \pm \sqrt{\frac{1}{2} - \frac{y}{\Lambda}},\tag{26b}$$

where in Eq. (26b) the plus and minus signs hold, respectively, for k = 0 and  $k = k_0$ , and  $\Delta$  is given by

$$\Delta = \sqrt{\left[\rho(1 - y^2)(c_0 + \beta_0)\right]^2 + 4y^2},\tag{27}$$

for k = 0, and by

$$\Delta = \sqrt{\left[\rho(1 - y^2)(c_0 - \beta_\lambda)\right]^2 + 4y^2},$$
 (28)

for  $k=k_0$ . The quantities  $\psi_+$  and  $\psi_-$  identify, respectively, the strongly and the weakly fluctuating fields in the  $\rho_1$ – $\rho_2$  plane.<sup>49</sup> In particular, for k=0, it holds

$$\lambda_{+} = \frac{\partial^{2}}{\partial \psi_{+}^{2}} \left( -\frac{\beta A}{V} \right), \tag{29a}$$

$$\lambda_{-} = \frac{\partial^{2}}{\partial \psi^{2}} \left( -\frac{\beta A}{V} \right). \tag{29b}$$

Hence, on the spinodal surface, the second derivative of the free energy along the strongly fluctuating field  $\partial^2 A/\partial \psi_+^2$  vanishes. This generalizes to mixtures the condition  $\partial^2 A/\partial \rho^2 = 0$  defining the spinodal curve in a one-component fluid. Similarly, the critical line(s) are the loci of the spinodal surface such that both the second and the third derivatives of A along  $\psi_+$  vanish, <sup>49</sup> i.e.,

$$\lambda_+ = 0, \tag{30a}$$

$$\frac{\partial \lambda_+}{\partial \psi_+} = 0. {(30b)}$$

From Eq. (25), we immediately obtain

$$\frac{\partial \lambda_{+}}{\partial \psi_{+}} = \cos \theta \frac{\partial \lambda_{+}}{\partial \rho_{1}} + \sin \theta \frac{\partial \lambda_{+}}{\partial \rho_{2}}.$$
 (31)

Equations (30) and (31) also give the critical line(s) on the  $\lambda$ -surface, provided that in Eq. (24),  $\beta_0$  is replaced by  $-\beta_{\lambda}$ , and Eq. (28) is used for  $\Delta$  instead of Eq. (27).

From the direction of strong fluctuation  $u_+ \equiv (\cos \theta, \sin \theta)$  in the  $\rho_1 - \rho_2$  plane, we can obtain the direction of strong fluctuation in the  $\rho - x$  plane. We introduce an angle  $\varphi$  such that  $\tan \varphi = \rho \, \delta x / \delta \rho$ . From  $\delta \rho = \delta \rho_1 + \delta \rho_2$  and  $\rho \, \delta x = -x \delta \rho_1 + (1-x) \delta \rho_2$ , we find

$$\tan \varphi = 1 - x - \frac{1}{1 + \tan \theta}.$$
 (32)

For a purely vapor–liquid transition,  $\varphi = 0$ , whereas for a purely mixing-demixing transition,  $\varphi = \pi/2$ .

Figures 2 and 3 show the critical lines in the  $\rho$ -x and  $\rho$ -T planes. The blue line is the critical locus of the spinodal instability at k = 0,

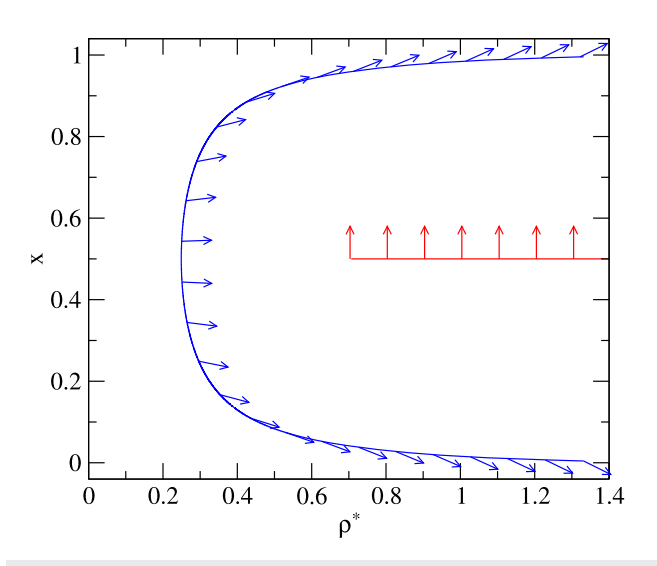


**FIG. 2.** Critical lines in the density-concentration plane. Blue line: Vapor–liquid critical line. Red line: Liquid-stripes critical line. The arrows indicate the direction of strong fluctuation (see text).

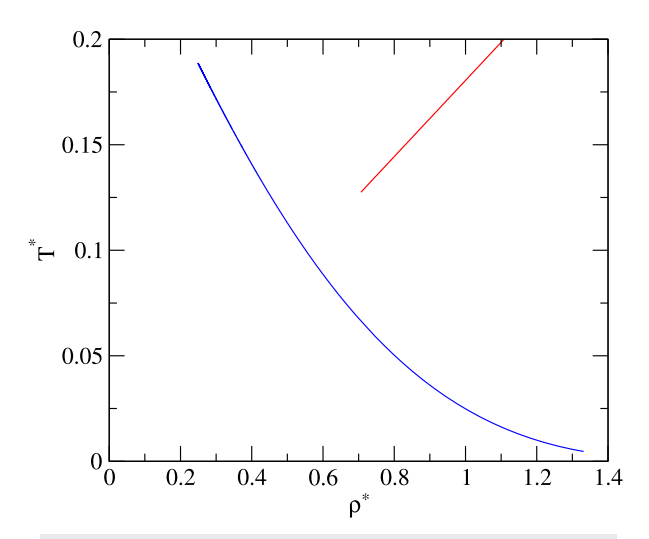


FIG. 3. Critical lines in the density-temperature plane. Lines as in Fig. 2.

whereas the red line is the critical locus of the Kirkwood instability at  $k = k_0$ . The arrows drawn along the lines in Fig. 2 display the direction of strong fluctuation according to Eq. (32).

Along the blue line, x = 1/2 corresponds to an azeotropic critical point, where the critical temperature reaches its maximum,  $T_a^* = 0.189$ , and the critical density reaches its minimum,  $\rho_a^* = 0.249$ . For  $T^* > T_a^*$ , the vapor-liquid transition and the related spinodal curve are absent, as observed in Sec. II. At x = 1/2, the transition is purely vapor-liquid and takes a partially mixing-demixing character as one moves toward x = 0 or x = 1. The line has been truncated at high density so as to discard its part lying inside the region bounded by the  $\lambda$ -surface, where macroscopic fluid-fluid phase separation becomes unstable.

Along the red line, the transition always involves purely concentration fluctuations. In fact, this line is nothing but the  $\lambda$ -line at equimolar concentration already studied in our former paper.<sup>36</sup> As discussed there, upon crossing it, the homogeneous fluid undergoes a second-order transition to a stripe phase, characterized by alternating domains richer in either component. The line meets the vapor-liquid coexistence curve of the equimolar mixture at the critical endpoint<sup>36</sup>  $T_e^* = 0.128$  and  $\rho_e^* = 0.706$ . At lower temperatures, criticality is preempted by a first-order transition.

The overall topology of the critical lines resembles one of the three types displayed by another class of symmetric mixtures where, at variance with the present case, attractive interactions also act between particles of the same species. 50-52 Nevertheless, there are two main differences in phase behavior between the two models: first, the mixtures considered in Refs. 50-52 do not exhibit inhomogeneous phases. They do feature a critical line at constant concentration x = 1/2, but that line corresponds to a mixing–demixing transition involving two macroscopic phases, rather than the formation of mesoscopic domains. Second, in that model, the pure components exhibit a vapor-liquid transition due to the intra-species attraction, and the vapor-liquid critical line connects their critical points at x = 0 and x = 1. Instead, in the present case, the vapor-liquid transition of the pure components is absent. As one moves away from the vapor-liquid transition at x = 1/2 by increasing or decreasing the concentration, the critical density rapidly increases and reaches values  $\rho^* \gtrsim 1$ , such that vapor-liquid phase separation will be most likely preempted by freezing. At the same time, the critical temperature decreases and goes to zero for  $x \to 0$  or  $x \to 1$ , although this is prevented by the critical line eventually hitting the  $\lambda$ -surface at a density near the close-packing value.

## IV. VAPOR-LIQUID TRANSITION

For the homogeneous mixture such that  $\rho_i(\mathbf{r}) \equiv \rho_i$ , Eq. (2) gives the standard mean-field approximation for the Helmholtz free energy,

$$\frac{\beta A_{\rm h}}{V} = \sum_{i=1}^{2} \rho_i (\ln \rho_i - 1) + \frac{\beta A_{\rm HS}^{\rm ex}}{V} - \beta_0 \rho_1 \rho_2, \tag{33}$$

where the subscript "h" refers to the homogeneous phase and the thermal wavelength  $\Lambda$  has been dropped, since it does not affect phase equilibria. In terms of the total density  $\rho$  and the rescaled concentration y, Eq. (33) reads

$$\frac{\beta A_{\rm h}}{V} = \rho \ln \frac{\rho}{2} - \rho + \frac{\rho}{2} \left[ (1+y) \ln (1+y) + (1-y) \ln (1-y) \right] 
+ \frac{\rho \eta (4-3\eta)}{(1-\eta)^2} - \frac{1}{4} \beta_0 \rho^2 (1-y^2),$$
(34)

where Eq. (5) for  $A_{\rm HS}^{\rm ex}$  has been used. From Eq. (34), the pressure P and the chemical potentials  $\mu_1$  and  $\mu_2$  of the two species are obtained. For ease of computation, we introduce the total chemical potential  $\mu \equiv \mu_1 + \mu_2$  and the relative chemical potential  $\Delta \mu \equiv \mu_1 - \mu_2$ . The following relations hold:

$$\beta P = -\frac{\beta A}{V} + \rho \frac{\partial}{\partial \rho} \left( \frac{\beta A}{V} \right), \tag{35a}$$

$$\beta \mu = 2 \frac{\partial}{\partial \rho} \left( \frac{\beta A}{V} \right) - \frac{2y}{\rho} \frac{\partial}{\partial \nu} \left( \frac{\beta A}{V} \right), \tag{35b}$$

$$\beta \Delta \mu = \frac{2}{\rho} \frac{\partial}{\partial y} \left( \frac{\beta A}{V} \right), \tag{35c}$$

from which we obtain

$$\beta P_{\rm h} = \rho \frac{1 + \eta + \eta^2 - \eta^3}{(1 - \eta)^3} - \frac{1}{4} \beta_0 \rho^2 (1 - y^2), \tag{36a}$$

$$\beta \mu_{\rm h} = 2 \ln \frac{\rho}{2} + 2 \left[ \frac{3 - \eta}{\left(1 - \eta\right)^3} - 3 \right] + \ln \left(1 - y^2\right) - \beta_0 \rho,$$
 (36b)

$$\beta \Delta \mu_{\rm h} = \ln \left( \frac{1+y}{1-y} \right) + \beta_0 \rho y. \tag{36c}$$

The coexistence region is obtained as usual by equating the pressure and chemical potentials of the coexisting phases, i.e.,  $P_{\rm A}$  =  $P_{\rm B}$ ,  $\mu_{\rm 1,A}$ =  $\mu_{1,B}$ , and  $\mu_{2,A} = \mu_{2,B}$ , where A and B are the two phases. Clearly, the equality of chemical potentials is equivalent to the conditions  $\mu_A = \mu_B$  and  $\Delta \mu_A = \Delta \mu_B$ .

Hereafter, we shall always refer to the coexisting phase of lower density as "vapor" and to that of higher density as "liquid," although the critical lines displayed in Sec. III imply that, for the mixture considered here, the density of the "vapor" can be much higher than the density of the vapor phase of, say, one-component Lennard-Joneslike fluids; moreover, at those high densities the transition will not be purely liquid-vapor in character.

## V. LANDAU THEORY OF INHOMOGENEOUS PHASES

To describe the inhomogeneous phases, we consider the strongly and weakly fluctuating fields  $\psi_+$  and  $\psi_-$  introduced in Sec. III. For an inhomogeneous phase,  $\psi_+$  and  $\psi_-$  are in general functions of r. Here, we assume that the inhomogeneity is brought into the system only by the strongly fluctuating field  $\psi_{+}$  and, therefore, make the following ansatz for  $\psi_{\perp}$  and  $\psi_{\perp}$ ,

$$\psi_{+}(\mathbf{r}) = \overline{\psi}_{+} + \frac{\rho}{2} \mathcal{A}\phi(\mathbf{r}),$$
 (37a)

$$\psi_{-}(\mathbf{r}) = \overline{\psi}_{-},\tag{37b}$$

where  $\overline{\psi}_+$  and  $\overline{\psi}_-$  are uniform quantities,  $\phi(\mathbf{r})$  is a periodic function of **r** with Fourier components only for  $k = k_0$ , and  $\mathcal{A}$  gives the amplitude of the modulation. From  $\rho_i = \int d^3 \mathbf{r} \rho_i(\mathbf{r})/V$  and Eq. (25), we obtain

$$\overline{\psi}_{+} = \cos\theta \, \rho_1 + \sin\theta \, \rho_2, \tag{38a}$$

$$\overline{\psi}_{-} = -\sin\theta \,\rho_1 + \cos\theta \,\rho_2,\tag{38b}$$

which, plugged into Eq. (25), finally give

$$\rho_1(\mathbf{r}) = \frac{\rho}{2} [1 + y + \cos\theta \mathcal{A}\phi(\mathbf{r})], \tag{39a}$$

$$\rho_2(\mathbf{r}) = \frac{\rho}{2} [1 - y + \sin \theta \mathcal{A} \phi(\mathbf{r})]. \tag{39b}$$

In the latter equations, it is understood that the angle  $\vartheta$  is that pertaining to  $k = k_0$ ; see Eqs. (26) and (28).

For a periodic function, it holds

$$\phi(\mathbf{r}) = \sum_{\mathbf{k}} e^{i\mathbf{k}\cdot\mathbf{r}} \hat{\phi}_{\mathbf{k}}, \tag{40}$$

where the sum runs over the vectors of the reciprocal lattice and  $\hat{\phi}_{\mathbf{k}}$ is the Fourier transform of  $\phi(\mathbf{r})$  defined as

$$\hat{\phi}_{\mathbf{k}} = \frac{1}{v} \int_{\mathcal{C}} d^3 \mathbf{r} e^{-i\mathbf{k}\cdot\mathbf{r}} \phi(\mathbf{r}), \tag{41}$$

where C denotes the primitive cell of volume v and, at variance with Eq. (10), the integral is not extended to the whole space but only to the primitive cell.

Following our *ansatz* for  $\phi(\mathbf{r})$ , we set

$$\hat{\phi}_{\mathbf{k}} = \frac{1}{q} \sum_{\mathbf{k}_0} \delta_{\mathbf{k}\mathbf{k}_0},\tag{42}$$

where the sum runs over the nearest-neighbor shell of the reciprocal lattice with coordination number *q*.

We now substitute Eq. (39) into the free-energy functional (2). We first focus on the interaction term. By going to Fourier space and taking Eq. (42) into account, this can be rewritten as

$$\frac{\beta}{2V} \sum_{i,j=1}^{2} \int d^{3}\mathbf{r} \int d^{3}\mathbf{r}' w_{ij}(\mathbf{r} - \mathbf{r}') \rho_{i}(\mathbf{r}) \rho_{j}(\mathbf{r}')$$

$$= \beta \sum_{\mathbf{k}} \hat{\rho}_{\mathbf{k},1} \hat{\rho}_{-\mathbf{k},2} \widetilde{w}(k)$$

$$= -\frac{1}{4} \beta_{0} \rho^{2} (1 - y^{2}) + \frac{1}{4} \beta_{\lambda} \rho^{2} \sin \theta \cos \theta \frac{\mathcal{A}^{2}}{q}.$$
(43)

To make further progress, we follow former investigations on SALR fluids<sup>53–55</sup> and expand the ideal-gas and the hard-sphere contributions in Eq. (2) in powers of A up to fourth order to obtain

$$\frac{\beta A}{V} = \frac{\beta A_{\rm h}}{V} + \frac{\Delta(\beta A)}{V},\tag{44}$$

where  $A_{\rm h}$  is the Helmholtz free energy of the homogeneous mixture given by Eq. (34), and  $\Delta(\beta A)$  is given by the Landau expression

$$\frac{\Delta(\beta A)}{V} = CA^2 + DA^3 + EA^4, \tag{45}$$

whose actual value is determined by minimization with respect to the amplitude A, which plays the role of the order parameter of the transition from the homogeneous to the inhomogeneous fluid. The expressions of the expansion coefficients C, D, and Eare given in the Appendix. In the following, we shall consider the usual candidates<sup>53,54</sup> for  $\phi(\mathbf{r})$ , namely, one-dimensional modulations (stripes), two-dimensional modulations on a triangular lattice (cylinders), and three-dimensional modulations (clusters) either on a body-centered cubic (bcc) or on a face-centered cubic (fcc) direct lattice. The corresponding expressions of  $\phi(\mathbf{r})$  are also reported in

Let us first consider the coefficient C of the quadratic term of Eq. (45). By substituting into Eq. (A1) the explicit expressions of  $\cos \theta$  and  $\sin \theta$  given by Eq. (26), we find

$$C = \frac{\rho}{8q(1-y^2)} \left[ 2 - \rho c_0 (1-y^2) - \Delta \right], \tag{46}$$

with  $\Delta$  given by Eq. (28). From Eq. (46), it is readily found that C is positive for  $|y| > |y_{\lambda}|$ , negative for  $|y| < |y_{\lambda}|$ , and vanishes for  $|y| = |y_{\lambda}|$ , where  $y_{\lambda}$  is the concentration on the  $\lambda$ -surface given by Eq. (19). Hence, upon entering the region bounded by the  $\lambda$ -surface, the uniform phase at A = 0 turns from a minimum to a maximum of the free energy and becomes unstable. This shows that the ansatz of Eq. (39) for the density profile is consistent with the analysis developed in Sec. II.

The coefficient E of the quartic term of Eq. (45) is always positive, whereas the coefficient D of the cubic term is always zero for the stripe and fcc phases. Moreover, at the equimolar concentration (y = 0), it also vanishes for the cylinder and bcc phases; see Eq. (A2). For D = 0, Eq. (45) describes a second-order transition that takes place at C = 0, i.e., on the  $\lambda$ -surface. It is shown in the Appendix that at equimolar concentration the stripe phase is always the inhomogeneous phase of lowest free energy, and at the  $\lambda$ -surface a second-order transition from the homogeneous fluid to the stripe phase occurs, as already established in our former study.<sup>36</sup> Moreover, the fcc phase is never found, because its free energy is always higher than that of the stripe phase, irrespective of the concentration. The latter result hinges on the assumption (42) for  $\hat{\phi}_k$  and on the expansion (45) of the Helmholtz free energy: in principle, other functional forms of the modulation or higher-order terms in  $\mathcal{A}$  might favor the fcc phase in some domain of the phase diagram. However, as we shall discuss in Sec. VI B, we do not find this to be the case for the system at hand.

At non-equimolar concentration, the cubic term D of Eq. (45)for the cylinder and bcc cluster phases is non-vanishing and may stabilize them with respect to stripes. In fact, for a given modulation amplitude A, stripes are energetically favored over cylinders and, afortiori, over clusters. However, when the difference in species concentration is sufficiently large, cylinders and clusters have to pay a smaller entropic penalty for domain formation because, compared to stripes, they offer a larger volume available to the more abundant species; see also Sec. VI B.

The presence of the cubic term D implies that the transition from the homogeneous to the inhomogeneous fluid at concentrations different from equimolar becomes first-order: before reaching the  $\lambda$ -surface at C = 0, the order parameter  $\mathcal{A}$  jumps discontinuously from A = 0 to  $A \neq 0$ . As shown in the Appendix, the transition from the homogeneous fluid to the bcc cluster phase preempts that from the homogeneous fluid to the cylinder phase. Hence, as the  $\lambda$ -surface is approached from the homogeneous region at non-equimolar concentration, the fluid undergoes a first-order transition to the bcc phase.

Inside the inhomogeneous region, the free energies of the stripe, cylinder, and bcc phases must be compared with one another to determine the domain of each phase; see the Appendix. As the difference in the concentrations of the two species becomes smaller, it is found that the bcc phase soon gives way to the cylinder phase, which is in turn replaced by the stripe phase at concentrations closer to equimolar. The domains of stability of each phase in the  $\rho$ -x plane will be graphically displayed in Sec. VI.

Neighboring phases are separated by a coexistence region to be determined by equating their pressures and chemical potentials obtained from Eq. (35), with A given by Eqs. (44) and (45). The determination of P,  $\mu$ , and  $\Delta\mu$  is straightforward, although tedious. At variance with the vapor-liquid equilibrium discussed in Sec. IV,

in the present case, the coexistence regions in the  $\rho$ -x plane turn out to be very narrow, to the point of being hardly distinguishable from the loci of equal free energy. Nevertheless, in the following, we shall display the coexistence regions, consistent with what we have performed for the vapor–liquid transition.

We note that in the free energy (44), the dependence on the well width  $\gamma$  comes about only via the quantities  $\beta_0$  and  $\beta_\lambda$  introduced in Sec. II. Specifically,  $\beta_0$  appears in Eq. (34) for the free energy  $A_h$  of the homogeneous mixture, and  $\beta_\lambda$  appears in the coefficients C, D, and E of the Landau free energy (45), given in Eqs. (A1)–(A3). Therefore, as already observed for the spinodal and  $\lambda$ -surfaces, within the present treatment, the dependence of the phase diagram on  $\gamma$  is completely accounted for by  $T^*$ .

Finally, we remark that the second-order character of the transition from the homogeneous fluid to the stripe phase at equimolar concentration discussed earlier is actually a shortcoming of the mean-field approximation. It has long been pointed out that transitions from a disordered to a periodic phase, such as those considered here, become first-order upon the inclusion of fluctuations. On the theoretical side, this has been discussed in detail both for one-component SALR fluids 53.57 and for binary mixtures. 28.47 For SALR fluids, further evidence of the fluctuation-induced first-order nature of this kind of transition has been provided by numerical simulations. 18.19 We shall return to possible effects of fluctuations on the qualitative features of the phase diagram in Sec. VI C.

#### VI. PHASE DIAGRAM

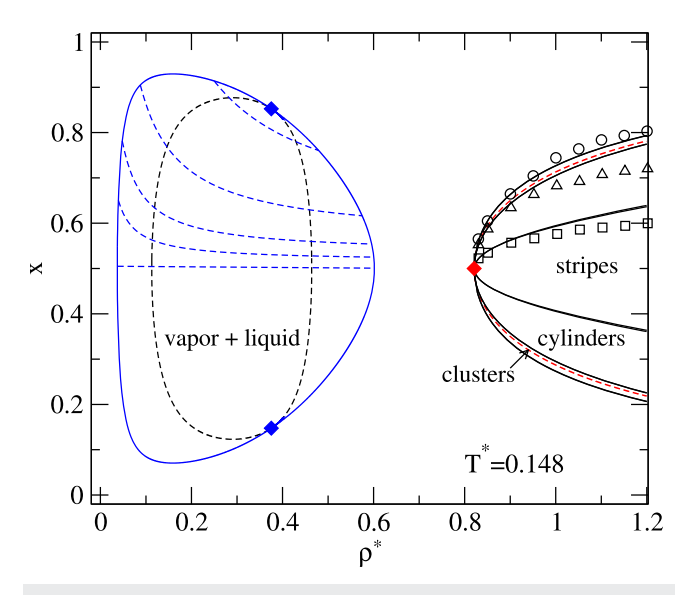
## A. Results from Landau theory

The mean-field phase diagrams in the  $\rho$ -x plane obtained by combining the results for the vapor-liquid transition with those of Landau theory for the transitions involving inhomogeneous phases are displayed for  $T^*$  = 0.148,  $T^*$  = 0.119, and  $T^*$  = 0.0889 in Figs. 4–6, respectively. These reduced temperatures correspond to  $\gamma$  = 0.5 and  $k_{\rm B}T/\varepsilon$  = 0.5, 0.4, 0.3.

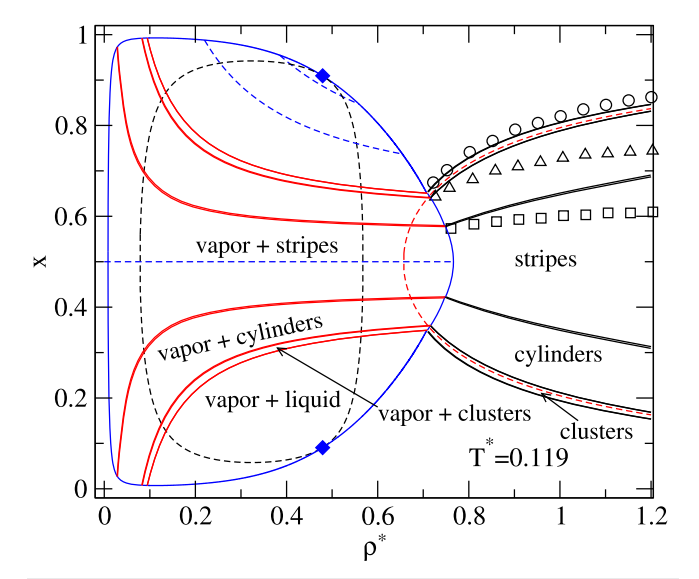
At such temperatures, both kinds of transitions are present. As discussed in Sec. III, for temperatures larger than the azeotropic critical temperature  $T_a^*=0.189$ , the spinodal instability and the related vapor–liquid transition disappear, and only the transitions from the homogeneous fluid to the inhomogeneous mesophases survive. However, in this temperature regime, these transitions are predicted to occur at very high density, where they might be preempted by crystallization.

Figure 4 shows that for  $T^*=0.148$  the liquid–vapor coexistence curve and the  $\lambda$ -line are disconnected, implying that the domain of the inhomogeneous mesophases can be accessed only from the high-density liquid. This is the scenario to be expected for temperatures smaller than  $T_a^*$  and larger than the endpoint temperature  $T_e^*=0.128$  (see Sec. III). As the temperature is decreased below  $T_e^*$ , the two curves intersect, and the domain bounded by their intersection becomes larger and larger, as shown in Figs. 5 and 6. In this regime, the vapor–liquid transition is partially preempted by a transition from the vapor to the inhomogeneous mesophases, whether they are clusters, cylinders, or stripes. At low temperatures, vapor-mesophase equilibrium occupies most of the coexistence region (see Fig. 6).

If A and B denote two phases at coexistence, all the states inside the coexistence region obtained by changing the relative abundance



**FIG. 4.** Phase diagram for reduced temperature  $T^*=0.148$  in the density-concentration plane according to the mean-field theory described in Secs. IV and V. Black dashed line: spinodal curve. Blue solid line: vapor–liquid coexistence curve. Blue dashed lines: tie lines connecting the vapor and liquid phases at coexistence. Blue diamonds: vapor–liquid critical points. Red dashed line:  $\lambda$ -line. Black solid lines: stripes–cylinders, cylinders–clusters, and clusters–fluid coexistence curves. On the scale of the figure, the corresponding coexistence regions are hardly distinguishable from a single curve. Red diamond: fluid–stripes critical point. The open symbols refer to the phase boundaries obtained from the numerical minimization of the free-energy functional (2), with no a *priori* assumptions on the form of the density profiles  $\rho_i(\mathbf{r})$  (see Sec. VI B). Squares: stripes–cylinders. Triangles: cylinders–clusters. Circles: clusters–fluid. The width of the coexistence regions is always much smaller than the symbol size. For ease of readability, only the points for x > 0.5 have been shown.



**FIG. 5.** Same as Fig. 4 for  $T^* = 0.119$ . The red solid lines mark the boundaries of the three-phase regions. On the scale of the figure, these regions are undistinguishable from a single curve.

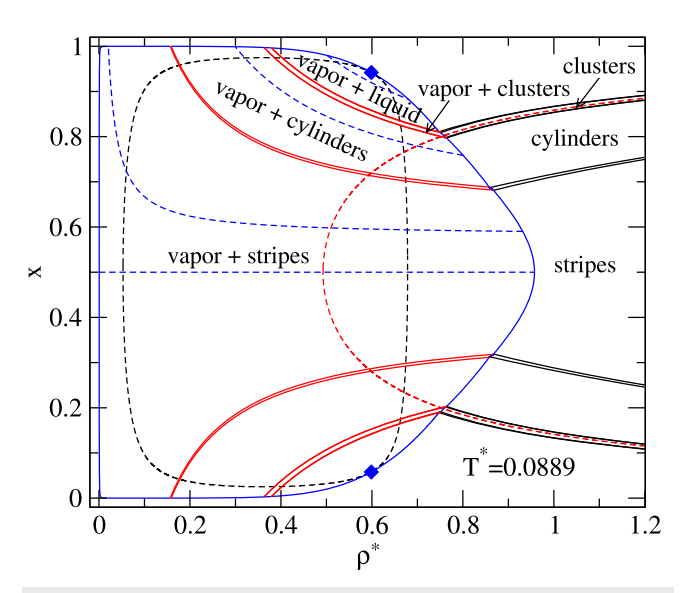


**FIG. 6.** Same as Fig. 5 for  $T^* = 0.0889$ . Only the results of Landau theory are shown. Here, the finite size of the vapor–stripes–cylinders three-phase region can be appreciated.

of A and B are at coexistence with one another. These states are connected by a *tie line* joining A to B. We denote by  $\rho_A$  and  $\rho_B$  the densities of the two phases at coexistence, by  $x_A$  and  $x_B$  their concentrations, and by  $N_A$  and  $N_B$  the number of particles in each phase, irrespective of their species. The relative abundance  $\bar{x} = N_A/(N_A + N_B)$  of phase A is given by the lever rule,

$$\bar{x} = \frac{v - v_{\rm B}}{v_{\rm A} - v_{\rm R}},\tag{47}$$

where  $v = 1/\rho$  is the specific volume of a generic state at equilibrium with A and B, and  $v_A$  and  $v_B$  are the specific volumes of A and B. The concentration x of such a state is

$$x = x_{A}\overline{x} + x_{B}(1 - \overline{x}) = x_{A}\frac{v - v_{B}}{v_{A} - v_{B}} + x_{B}\frac{v_{A} - v}{v_{A} - v_{B}},$$
 (48)

i.e.,

$$x = \frac{\rho_{\rm A}\rho_{\rm B}}{\rho_{\rm B} - \rho_{\rm A}} (x_{\rm A} - x_{\rm B}) \frac{1}{\rho} + \frac{\rho_{\rm B}x_{\rm B} - \rho_{\rm A}x_{\rm A}}{\rho_{\rm B} - \rho_{\rm A}}.$$
 (49)

Equation (49) gives the tie lines in the  $\rho$ -x plane, except in the case of a purely mixing-demixing transition such that  $\rho_A = \rho_B$ , for which one has  $\rho = \rho_A = \rho_B$  for every x. Some tie lines are shown as blue dashed lines in Figs. 4–6. We remark that they are not straight lines, except for the azeotropic mixture at x = 0.5, for which the tie line is horizontal, since the same concentration x = 0.5 is shared by all the states at coexistence. As a consequence, a line at constant  $x \neq 0.5$  inside the coexistence region intersects different tie lines as  $\rho$  changes. This implies that, at variance with one-component fluids, the densities at coexistence  $\rho_A$  and  $\rho_B$  (as well as  $x_A$  and  $x_B$ ) depend on  $\rho$ .

We also observe that at low temperatures, as soon as the concentration gets slightly above or below x = 0.5, the vapor phase at coexistence consists almost entirely of the more abundant species

(see Fig. 6). The reason for this is that the phase at higher density takes more advantage of the attractive interaction, because the internal energy per particle scales as  $\sim \rho$ . Since in the mixture at hand the attraction acts only between particles of different species, the system finds it energetically convenient to keep the concentration of the phase at higher density closer to equimolar than the average concentration. As a consequence, the excess particles of the more abundant species are expelled to the phase of lower density. This behavior agrees with the results of numerical simulations. 45

The points at which the vapor-liquid coexistence curve touches the spinodal curve are the critical points of the vapor-liquid transition, which lie on the vapor-liquid critical line of Fig. 2. When approaching those points, the densities and concentrations of the coexisting phases become the same, as shown by the behavior of the tie lines.

In the low-temperature regime displayed in Figs. 5 and 6, the vapor can coexist not only with the liquid but also with different mesophases. If we consider two neighboring coexistence regions such that the vapor coexists with some phase A in one region and with another phase B in the other, then the boundary between the two regions consists of a triple point, at which the vapor, phase A, and phase B coexist together. In the  $\rho$ -x plane, this triple point appears as a three-phase domain bounded by three tie lines connecting the vapor with A, the vapor with B, and A with B, which have been drawn in red in Figs. 5 and 6. These three-phase domains, although very narrow, are clearly distinguishable at the boundary between the vapor-stripes and vapor-cylinders coexistence regions at the lowest temperature considered (see Fig. 6). In other cases, they appear as lines on the scale of the figures because of the very small differences in the densities and concentrations of phases A and B.

## B. Comparison with numerical minimization

The previous analysis is based on three additional assumptions in addition to the mean-field approximation, namely, Eq. (39) for the density profiles, the *ansatz* (42) for the function  $\phi(\mathbf{r})$  describing their modulations, and the Landau expansion (45) of the free energy in powers of the modulation amplitude  $\mathcal{A}$ . As discussed in Sec. V, the description of the inhomogeneous phases that results from those assumptions appears to be reasonable in the neighborhood of the  $\lambda$ -line. However, it may become inaccurate as one moves away from it, entering more deeply into the inhomogeneous domain.

We have then considered the grand potential functional  $\Omega = A - \sum_{i=1}^2 \mu_i N_i$  with A given by Eq. (2) and performed some minimization runs of  $\Omega$  using the purely numerical algorithm already adopted in former investigations.  $^{36,43,44}$  Unlike the Landau theory discussed in Sec. V, this algorithm does not make any assumptions about the functional form of the density profiles  $\rho_i(\mathbf{r})$ , except for their periodicity. The unit cell was sampled on a grid consisting of  $128^3 = 2\,097\,152$  points, and the minimization was carried out with respect to both the values taken by  $\rho_i(\mathbf{r})$  at those points and to the cell axes.

In Sec. V, it was pointed out that, within the Landau theory described there, the dependence of the phase diagram on the well width  $\gamma$  is accounted for by incorporating  $\gamma$  in the definition of reduced temperature,  $T^* = 1/\beta^*$ , with  $\beta^* = \beta \varepsilon (1 + \gamma)^3$ . Here, we remark that, under the assumption of periodicity, this property is

intrinsic to the mean-field treatment based on the free-energy functional (2), irrespective of whether  $\rho_i(\mathbf{r})$  is parameterized analytically or not. If we denote by  $\mathbf{A}$  the matrix of the primitive vectors of the lattice, we may set

$$\rho_i(\mathbf{r}) = \rho_i(\mathbf{A} \cdot \mathbf{s}) \equiv f_i(\mathbf{s}), \tag{50}$$

where  $\mathbf{s}$  is a vector that varies in a cube Q of unit edge. The free energy functional then assumes the form

$$\frac{\beta A[\rho_{1}(\mathbf{r}), \rho_{2}(\mathbf{r})]}{V} = \int_{Q} d^{3}\mathbf{s} \frac{\beta A_{\text{IID}}^{\text{mix}}}{V} (f_{1}(\mathbf{s}), f_{2}(\mathbf{s})) 
+ \int_{Q} d^{3}\mathbf{s} \frac{\beta A_{\text{HS}}^{\text{ex, mix}}}{V} (f_{1}(\mathbf{s}), f_{2}(\mathbf{s})) 
+ \beta \sum_{\mathbf{r}} \hat{f}_{1}(\mathbf{n}) \hat{f}_{2}(-\mathbf{n}) \widetilde{w}(k_{\mathbf{n}}),$$
(51)

where  $\mathbf{n} \equiv (n_1, n_2, n_3)$  is a vector with integer components and  $\hat{f}_i(\mathbf{n})$  is given by

$$\hat{f}_i(\mathbf{n}) = \int_{\Omega} d^3 \mathbf{s} e^{-2\pi i \mathbf{n} \cdot \mathbf{s}} f_i(\mathbf{s}). \tag{52}$$

Hence,  $f_i(\mathbf{s})$  and  $\hat{f}_i(\mathbf{n})$  depend solely on the values taken by the density profiles inside the cell, irrespective of the lattice. The information on the lattice is conveyed only via the  $k_{\mathbf{n}}$  at which  $\widetilde{w}(k)$  is evaluated. By virtue of Eq. (14), if we rescale the lattice by introducing the dimensionless wave vectors  $\mathbf{k}_{\mathbf{n}}\xi$ , then the dependence on the interaction range in Eq. (51) is entirely contained in the inverse reduced temperature  $\beta^*$ . The density profiles corresponding to the same values of  $\beta^*$ ,  $\rho^*$ , and x coincide, provided they are plotted in terms of the rescaled position  $\mathbf{r}/\xi$ . This holds not only for the squarewell interaction (1) but also for any tail interaction w(r) described by a generic function w(r) an energy scale  $\varepsilon$ , and a range  $\xi$  such that  $w(r) = \varepsilon u(r/\xi)$ .

In Figs. 4 and 5, the results of the numerical minimization are compared with the phase diagram predicted by the Landau theory at reduced temperatures  $T^*=0.148$  and  $T^*=0.119$ . On purely qualitative grounds, the inhomogeneous mesophases are the same as those described in Sec. VI A: as the concentration departs from x=0.5, we find first a stripe phase on a one-dimensional lattice, then a cylinder phase on a triangular lattice, and finally a cluster phase on a bcc lattice. In order to investigate the possible occurrence of other mesophases, we performed several runs at  $T^*=0.148$  starting from an *ad hoc* trial density profile describing either an fcc cluster phase or a gyroid bicontinuous phase. While those phases were found to describe local minima of  $\Omega$  for some densities and concentrations, they were always superseded by either the stripe, the cylinder, or the bcc phase, which provided a lower  $\Omega$  for the same chemical potentials.

This behavior is different from that previously observed in SALR fluids<sup>44</sup> and binary mixtures of particles interacting via softcore Gaussian potentials,<sup>43</sup> whose phase portrait also features more exotic structures, including the gyroid and, in the SALR case, non-bcc cluster phases. In fact, the stability of those mesophases rests on the Fourier spectrum of the potential beyond the nearest-neighbor shell and, therefore, depends on the specific interaction considered.

A pictorial representation of the stripe, cylinder, and bcc cluster phases obtained from the numerical minimization is given in

Figs. 7–9, which were produced by the VESTA software.<sup>58</sup> They correspond to the same temperature  $T^* = 0.148$  and  $\rho^* = 0.953$ , x = 0.451 for the stripes,  $\rho^* = 0.953$ , x = 0.401 for the cylinders, and  $\rho^* = 0.951$ , x = 0.301 for the bcc clusters.

It is worth pointing out that, according to both the numerical minimization of the grand potential discussed here and the analytic representation of the density profiles presented in Sec. V, the cylinder and bcc cluster phases do not consist of alternating arrays of localized cylinders or clusters of the two species. Actually, these structures are formed only by the less abundant species, whereas the more abundant species percolates into the space left available by the less abundant species. When the difference in species concentration is sufficiently large, this makes cylinders entropically favored over stripes, and clusters entropically favored over cylinders. In the double-periodic cylinder phase, the density peaks of the more abundant species are located at the sites of a honeycomb lattice. In the triply periodic bcc phase, the more abundant species arranges into a bicontinuous phase sometimes referred to as "plumber's nightmare." <sup>59</sup> The same behavior was observed in the cylinder and bcc phases of the Gaussian mixture considered in Ref. 43.

Despite qualitative similarities, Figs. 4 and 5 show that the analytic and numerical treatments of the inhomogeneous phases display significant quantitative differences: while the boundary between the homogeneous fluid and the bcc cluster phase is similar in the two approaches, according to the numerical minimization, the inner

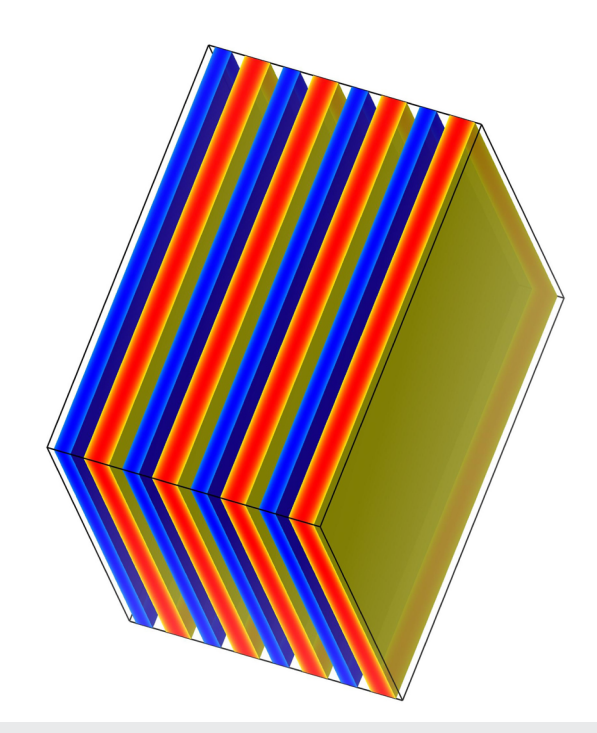


**FIG. 7.** Section of the density profiles of the stripe phase at  $T^* = 0.148$ ,  $\rho^* = 0.953$ , and x = 0.451. Yellow to red shades refer to the density profile  $\rho_1(\mathbf{r})$  of the more abundant species 1, and light to dark blue shades refer to the density profile  $\rho_2(\mathbf{r})$  of the less abundant species 2.

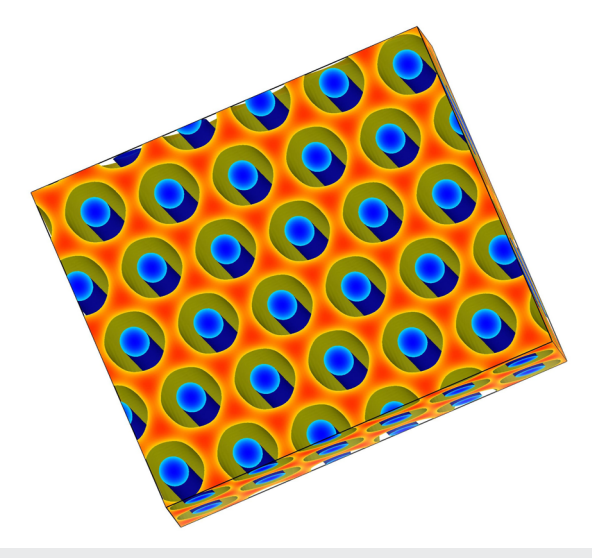


**FIG. 8.** Same as Fig. 7 for the cylinder phase at  $T^* = 0.148$ ,  $\rho^* = 0.953$ , and x = 0.401.

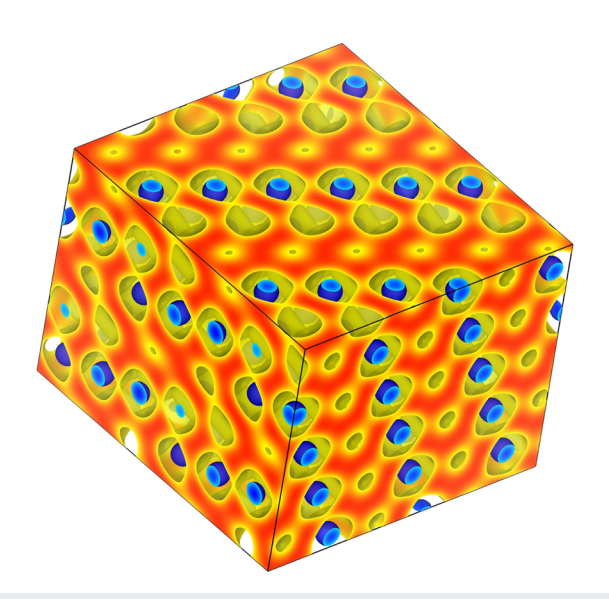


**FIG. 9.** Same as Fig. 7 for the bcc cluster phase at  $T^* = 0.148$ ,  $\rho^* = 0.951$ , and x = 0.301.

boundary of the bcc domain at high density is moved to concentrations closer to equimolar. As a consequence, the cylinder region is also shifted toward equimolar concentration, thereby squeezing the stripe region. The result is a considerable widening of the bcc domain at the expense of the stripes, whose domain is much narrower than predicted by the Landau approach.

Figure 5 does not display the equilibrium curves between the vapor and the inhomogeneous phases given by the numerical minimization, but we expect them to be very similar to those of the Landau theory already shown. In fact, at the temperature considered

in the figure, the densities of the inhomogeneous phases at coexistence with the vapor are relatively low so the analytic and numerical approaches do not differ much. We anticipate that this will no longer be the case at lower temperature, such as that in Fig. 6, at which the densities of the inhomogeneous phases at coexistence are higher.

In light of the quantitative discrepancies between the phase behavior of the two approaches, it is natural to ask how their respective density profiles compare. This comparison is presented in Figs. 10 and 11. Each figure displays, for three states, the concentration profiles  $x(r) = \rho_2(r)/\rho(r)$  (blue lines) and the total density  $\rho(r)$  (red lines) along a line connecting nearest-neighbor peaks of the less abundant species 2, according to both the Landau theory and the numerical minimization. The figures refer to the same reduced temperature  $T^*=0.125$ , intermediate between those of Figs. 4 and 5, and two different densities  $\rho^*\simeq 0.8$  and  $\rho^*\simeq 1.15$  (in the panels of each figure, the densities are not exactly the same, since they were obtained a posteriori by minimization in the grand canonical ensemble). The concentrations were chosen in such a way that, for each  $T^*$ 

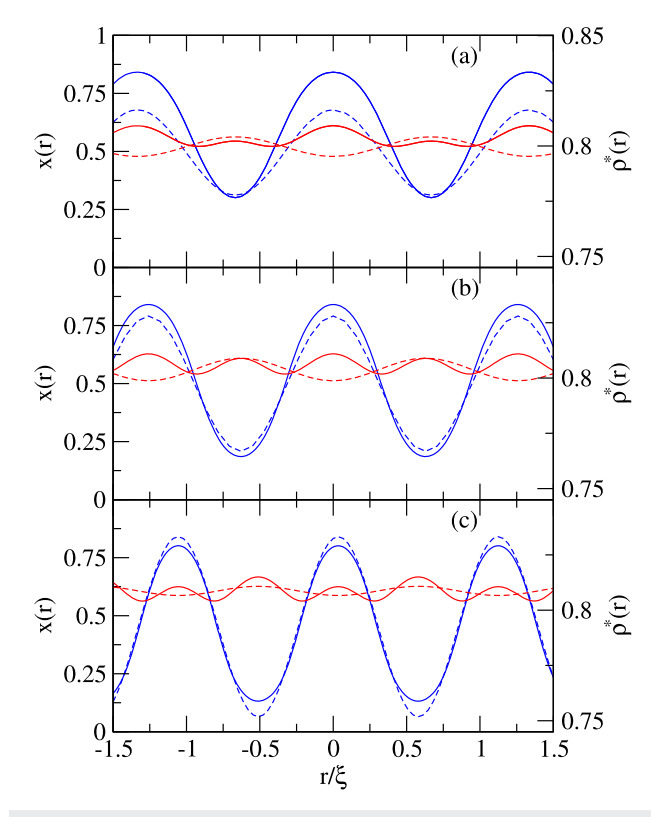


**FIG. 10.** Concentration profiles x(r) (blue curves) and total density profiles  $\rho^*(r)$  (red curves) at  $T^*=0.125$ ,  $\rho^*\simeq0.8$ , and different concentrations x for the cluster, cylinder, and stripe phases along the direction connecting nearest-neighbor peaks of the minority species 2. Solid and dashed curves refer, respectively, to the numerical minimization of the grand potential functional and to the analytical results of the Landau theory described in Sec.  $\vee$ . Panel (a):  $\rho^*=0.804$ , x=0.312, bcc clusters. Panel (b):  $\rho^*=0.806$ , x=0.353, cylinders. Panel (c):  $\rho^*=0.809$ , x=0.452, stripes.

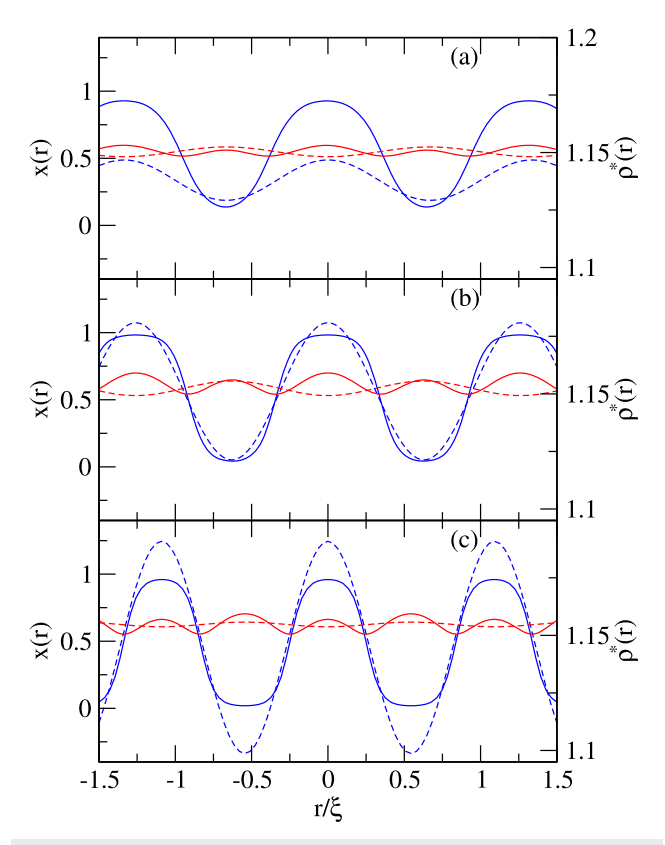


**FIG. 11.** Same as Fig. 10 at  $T^*=0.125$  and  $\rho^*\simeq 1.15$ . Panel (a):  $\rho^*=1.152$ , x=0.187, bcc clusters. Panel (b):  $\rho^*=1.154$ , x=0.306, cylinders. Panel (c):  $\rho^*=1.155$ , x=0.453, stripes. Note the unphysical values of x(r) predicted by the analytical theory in panels (b) and (c).

and  $\rho^*$ , the analytic and numerical approaches predict the same kind of phase, either stripes, cylinders, or bcc clusters.

We first observe that, for all the states considered, the period of the concentration profiles obtained via the numerical minimization (blue solid curves) agrees almost perfectly with that of the analytic theory (blue dashed curves) which, according to Eq. (42), is determined solely by the wave vector  $k_0$  of the maximum of  $\widetilde{w}(k)$ . However, as displayed in panel (a) of both Figs. 10 and 11, in the cluster phase, the analytic theory strongly underestimates the amplitude of the oscillations. Specifically, while the minima of x(r) are in good agreement with the numerical results, its maxima are underestimated. As a consequence, the tendency toward segregation into domains where one of the species is much more abundant than the other is weaker than predicted by the numerical minimization. Indeed, according to the analytic results, in panel (a) of Fig. 11, x(r)is always smaller than 0.5, thereby implying that the local concentration 1 - x(r) of the more abundant species 1 is always larger than that of species 2. Even in panel (a) of Fig. 10, where the analytic x(r) reaches values above 0.5, the peaks of 1-x(r) are still larger than those of x(r). Instead, according to the numerical results, the converse is true: the higher concentration peaks actually pertain to the less abundant species 2. This does not imply any contradiction because, as pointed out earlier, the less abundant species is localized

in the neighborhood of the lattice sites, whereas the more abundant species percolates through all the remaining space.

Turning to the concentration profiles of the cylinder and stripe phases displayed in panels (b) and (c), at the lower density  $\rho^* \simeq 0.8$  of Fig. 10, the analytic theory slightly underestimates the amplitude of the oscillations for the cylinders and slightly overestimates it for the stripes. Nevertheless, overall the analytic and numerical concentration profiles are in fair agreement, as the latter do not deviate much from a sine-like wave.

However, at the higher density  $\rho^* \simeq 1.15$  of Fig. 11, there is a marked change in the behavior of the numerical predictions: as already observed for SALR fluids<sup>44</sup> as well as for the mixture at hand at equimolar concentration, 36 the maxima and the minima of x(r)become flatter, with the minima nearly vanishing. This situation corresponds to a sequence of alternating domains populated almost exclusively by either species, separated by rather sharp interfaces. Such a strong-segregation regime cannot be satisfactorily described by the sine-like modulations of the analytic theory. In fact, the growth of the modulation amplitude A can even lead to unphysical values of x(r), either negative or larger than unity, as displayed in panels (b) and (c) of Fig. 11. In the free-energy functional (2), this occurrence is forbidden by the ideal-gas term (3), whereas this is not the case for its expansion (45), which formally exists for every value of A. However, as A grows, the expansion itself is bound to become inaccurate.

We are then led to conclude that the permanence of the cylinder and, even more, of the stripe phases in the regime where the difference between the concentrations of the two species is large is an artifact of the analytic theory, which fails to reproduce the actual shapes of the density profiles at high density.

As for the total density profiles  $\rho(r)$  (red curves in Figs. 10 and 11), they also display oscillations. The period of the analytic and numerical  $\rho(r)$  (dashed and solid curves, respectively) is the same, and in both cases, it is the same as that of x(r). However, the numerical  $\rho(r)$  has a richer structure: specifically, it features modulations that alternate oscillations of larger and smaller amplitude, so that the distance between neighboring peaks is actually half of that of the analytic  $\rho(r)$ . Moreover, the analytic theory always underestimates the amplitude of the oscillations compared to the numerical results. That said, the most relevant feature of  $\rho(r)$  is that, unlike the local concentration x(r), its oscillations are always very small: for all the cases displayed in Figs. 10 and 11, the relative amplitude  $|\rho(r) - \rho|/\rho$ is well below 1%. Hence, in the inhomogeneous phases, concentration fluctuations always dominate over density fluctuations, with the latter rigorously vanishing along the fluid-stripes critical line at x = 0.5 displayed in Fig. 2.

## C. Comparison with simulation results

In recent investigations, <sup>35,36,45</sup> the phase behavior of the mixture considered here was addressed by numerical simulation. Here, we discuss how the present results compare to those obtained there.

In Fig. 12, the liquid–vapor coexistence curves predicted by the free-energy functional (2) are compared to those obtained by Gibbs Ensemble Monte Carlo (GEMC) simulations at concentrations  $x = 0.5^{35,36}$  and  $x = 0.3^{45}$  in panels (a) and (b), respectively. We recall that the description of the liquid–vapor transition resulting from functional (2) is that of standard mean-field theory.

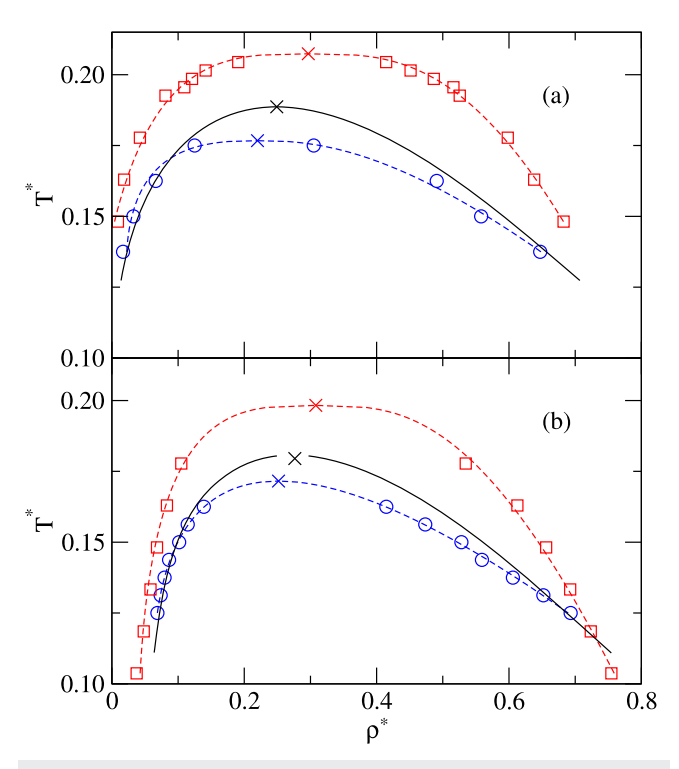


**FIG. 12.** Liquid–vapor coexistence curves in the density-temperature plane at x=0.5 (panel (a)) and x=0.3,  $\rho^*=0.25$  (panel (b)). Black solid curve: theory. Blue circles: simulation,  $\gamma=1$ . Red squares: simulation,  $\gamma=0.5$ . The dashed lines are the best fits of the simulation data based on the law of rectilinear diameters and the scaling law for the density difference between liquid and vapor. The crosses indicate the position of the critical point.

As observed in Sec. VI A, for  $x \neq 0.5$ , the densities at coexistence depend on the total density  $\rho$ . The curves for x = 0.3 displayed in panel (b) correspond to the isochore  $\rho^* = 0.25$ . Since this value is somewhat smaller than the critical density  $\rho_c^* = 0.276$  predicted by the theory for x = 0.3, the vapor and liquid branches of the theoretical curve do not join at the critical point but end at a temperature slightly higher than the critical value, leaving a small gap that includes the critical density. Similar considerations would also hold for the simulation results, even though in that case the highest temperatures investigated are still below the endpoint of the transition. However, according to the theoretical results, the isochore at hand is rather close to the critical one, and we expect that this will also be the case for the simulations. Therefore, we reckon that a sensible estimate of the simulation critical points for x = 0.3 can be obtained by the standard procedure of fitting the simulation data to the scaling law for the density difference between liquid and vapor and the law of rectilinear diameters, as performed for x = 0.5.

The behavior for x = 0.3 is similar to that observed for x = 0.5. As noted earlier, in mean-field theory, the effect of the well width  $\gamma$  is already taken into account by the present definition of the reduced temperature  $T^* = k_{\rm B}T/[\varepsilon(1+\gamma)^3]$ , so the coexistence curves corresponding to different values of  $\gamma$  are predicted to collapse on the same curve, provided the temperature is rescaled accordingly. However, the simulation results show that this is not the case, since

the curves for  $\gamma=1$  and  $\gamma=0.5$  differ markedly from each other, and both of them differ from the mean-field curve. In fact, the mean-field theory overestimates the critical temperature  $T_c$  for  $\gamma=1$  and underestimates it for  $\gamma=0.5$ . The discrepancies are larger for  $\gamma=0.5$ , whose simulation coexistence curves are much flatter than the mean-field ones.

These findings qualitatively agree with the behavior of one-component square-well fluids for which, as  $\gamma$  decreases,  $k_{\rm B}T_{\rm c}/\varepsilon$  must obviously decrease and eventually vanish for  $\gamma \to 0$ . In this limit,  $T_{\rm c}$  follows Noro and Frenkel's extended law of corresponding states, which assumes a constant value for the second virial coefficient at the critical temperature  $B_2(T_{\rm c})^{61}$  and yields a dependence of  $T_{\rm c}$  on  $\gamma$  different from that of mean-field theory. By contrast, for  $\gamma=2$ , the mean-field coexistence curve was found to agree closely with simulation,  $^{36}$  and we expect that this will be the case a fortiori for wider wells such that  $\gamma>2$ . In this regime, the mean-field scaling  $k_{\rm B}T_{\rm c}/\varepsilon\sim (1+\gamma)^3$  will most likely be fulfilled.

The study of the inhomogeneous phases at  $x \neq 0.5$  by numerical simulations was addressed in Ref. 45. An extended comparison between the present results and those obtained there is hindered by the fact that Ref. 45 focuses mostly on the description of the crystal structures into which the particles arrange at high density, whereas the LDA used here for the hard-sphere contribution to the free-energy functional (2) is unable to describe freezing on an atomic scale. A tentative comparison is presented in Fig. 13, where two sections at constant concentration x = 0.3 of the phase diagrams obtained by Landau theory for  $T^* = 0.0625$  and  $T^* = 0.125$  are shown together with the simulation results for y = 1 at the same

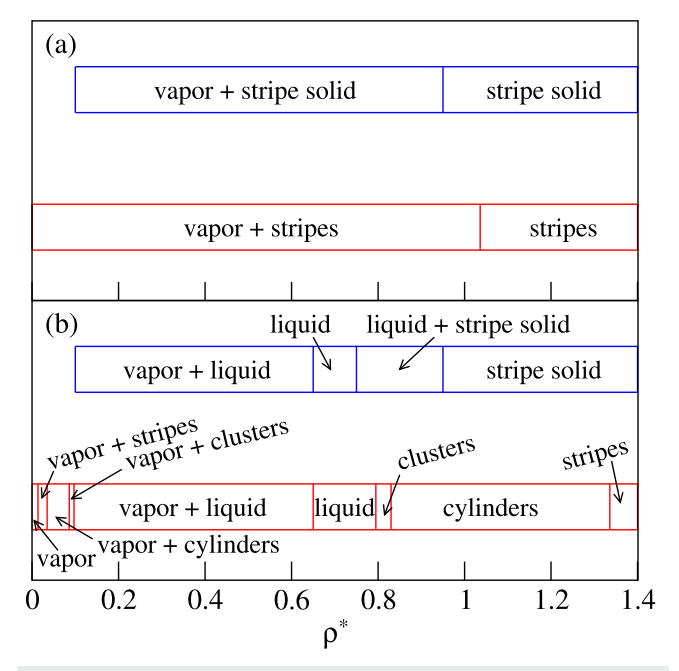


**FIG. 13.** Phase diagram at concentration x=0.3. Panel (a):  $T^*=0.0625$ . Panel (b):  $T^*=0.125$ . Red boxes: Landau theory. Blue boxes: simulation results for  $\gamma=1.45$ 

x and  $T^*$ , corresponding to the values  $k_BT/\varepsilon = 0.5$  and  $k_BT/\varepsilon = 1$  displayed in Fig. 11(c) of Ref. 45.

At  $T^* = 0.0625$  [see panel (a)], simulation and theory agree at least qualitatively, as they both predict a vapor phase at low density and a stripe phase at high density, separated by a wide vapor–stripe coexistence region. According to the simulation, particles within the stripes form an fcc solid, 45 which is not surprising given their rather high density, while theory is silent as to the short-range arrangement of the particles, since it is unable to distinguish a stripe fluid from a stripe solid.

At the higher temperature  $T^* = 0.125$  [see panel (b)], both simulation and theory predict the occurrence of a liquid phase at intermediate densities, which was absent at  $T^* = 0.0625$ . At low density, the liquid coexists with the vapor, while at high density it coexists with the inhomogeneous phases. The liquid and vapor-liquid coexistence regions predicted by theory are in reasonable agreement with the simulation results. However, simulation and theory differ considerably when one turns to inhomogeneous phases. Indeed, according to simulation, the only inhomogeneous phase is the stripe solid already found at  $T^* = 0.0625$ , while theory yields not only stripes but also cluster and cylinder phases. At low density, these phases coexist with the vapor and give rise to a narrow sequence of coexistence regions located between the vapor and the vapor-liquid domains, which would probably be hard to detect by simulation. Nevertheless, at high density, the cylinder phase is predicted to occur in a wide domain and should be easily detectable.

The above-mentioned results pertain to the analytic description of the inhomogeneous phases based on Landau theory, but treatment based on the purely numerical minimization of the free-energy functional (2) would most likely lead to even larger discrepancies between simulation and theory because, as discussed in Sec. VI B, the numerical minimization predicts a narrower stripe domain compared to Landau theory.

A possible reason for these discrepancies is that the present theory hinges on the mean-field approximation that, as such, disregards fluctuations. As recalled in Sec. V, upon inclusion of fluctuations, the transition from the homogeneous fluid to the periodic mesophases becomes first-order also for x=0.5. However, fluctuations are likely to affect the phase diagram also in other respects. In the mean-field description, an isothermal section of the phase diagram always displays all kinds of mesophases, be they stripes, cylinders, or clusters (see Figs. 4–6). A similar behavior is found in monodisperse SALR fluids, where all inhomogeneous phases coalesce at the top of the  $\lambda$ -line in the  $\rho$ -T plane. <sup>44,53</sup>

However, simulation results for SALR fluids <sup>18,19</sup> show that fluctuations change the topology of the phase diagram in such a way that cylinders appear at a lower temperature than stripes, and clusters also appear at a lower temperature than cylinders. As a consequence, in a certain temperature interval, the only mesophase that survives is the stripe phase. This scenario is also supported by theoretical calculations beyond the mean-field level.<sup>57</sup> We are not in a position to state that a similar effect takes place for sure in the present system, but if it does, then this could explain why the cylinder and cluster phases predicted by the theory are not found in the simulations.

In addition, we should bear in mind the insensitivity of functional (2) to the interaction range. As observed in Sec. VI B, the reduced density profiles  $\rho_1^*(\mathbf{r})$  and  $\rho_2^*(\mathbf{r})$  at different  $\gamma$ , but at the same  $\rho^*$ , x, and  $T^*$ , coincide, provided they are regarded as functions

of  $\mathbf{r}/\xi$ . This law of corresponding states might provide a sensible description of the system for relatively wide wells but is bound to fail for narrow wells. In fact, for  $\gamma \lesssim 0.5$ , which is the smaller  $\gamma$  considered in Ref. 45, the distance between neighboring density peaks of different species would become less than the hard-sphere diameter  $\sigma$ , which is clearly unphysical. Even for the value  $\gamma = 1$  to which Fig. 13 refers, this distance is just on the order of  $\sigma$ . In such a regime, stripes actually consist of layers of atomic thickness, cylinders of rows of particles piled on top of each other, and the very notion of a spherical cluster becomes questionable since it would reduce to a single particle. Clearly, these structures cannot be regarded as a continuum on an atomic scale and might compete with those favored by steric hindrance, leading to new crystal phases. The description of these arrangements requires a realistic treatment of inhomogeneity on length scales  $\sim \sigma$ , which is beyond the LDA used here.

## VII. CONCLUSIONS

We have presented an investigation of the phase diagram of a model hard-sphere mixture consisting of two species of particles of equal diameter  $\sigma$ , with a square-well attraction acting only between different species. The study was carried out by DFT in the meanfield approximation and generalizes to generic species concentration x a former DFT study of the same mixture at equimolar concentration x = 0.5.<sup>36</sup> A particularly interesting feature of this model, which had already been established in the equimolar case 35,36 is that, unlike one-component SALR fluids, where mesophase formation preempts liquid-vapor phase separation, its phase diagram displays both transitions. Hence, depending on the temperature, mesophases can coexist with both the liquid and the vapor. This behavior does not occur in any model mixture leading to spontaneous pattern formation. In such mixtures, the phase diagram is generally more sensitive to the details of the interactions than in the one-component SALR or similar models. For example, in the equimolar mixture with SALR and inverse-SALR interactions considered in Ref. 28, the liquid-vapor transition is preempted by the onset of the mesophases, as in monodisperse SALR fluids.

Considering concentrations other than equimolar considerably enriches the phase portrait of the mixture. In fact, the equimolar concentration corresponds to the special case of an azeotropic mixture, such that the coexisting phases also have the same concentration, x=0.5. In this respect, the equimolar mixture behaves as a one-component fluid, whose phase diagram can be described in terms of density and temperature alone. This is no longer true for  $x \neq 0.5$ , because then the coexisting phases differ not only in density but also in concentration and, unlike in the azeotropic case, those densities and concentrations depend on the overall density and concentration of the mixture. Here, in particular, as soon as the overall concentration deviates from x=0.5, the concentrations of the coexisting liquid and vapor phases become very different, with the vapor phase being much richer in the more abundant species than the liquid.

The spectrum of the inhomogeneous mesophases is also wider than in the equimolar case. While at x = 0.5 only stripe-like density modulations are observed,  $^{35,36}$  here we find that moving off x = 0.5 stabilizes doubly periodic and, at larger or smaller x, triply periodic modulations, consisting, respectively, of cylinders arranged on a triangular lattice and spherical clusters arranged on a bcc lattice.

These domains are populated mainly by the less abundant species, while the more abundant species fill the region between them, similarly to what is observed in binary mixtures of particles interacting via soft-core Gaussian potentials.<sup>43</sup>

Stripe, cylinder, and cluster phases are commonly found in mesophase-forming fluids, <sup>6,44,53,54</sup> as their occurrence rests on rather general properties of the Fourier spectrum of the interaction. Even though we should recall that, according to both simulation <sup>18,19</sup> and theoretical studies, <sup>57</sup> in SALR fluids, fluctuations shift the cylinder and cluster domains to lower temperatures compared to stripes. Other, more exotic structures, such as, e.g., the gyroid <sup>19,44,53,54</sup> or the double diamond, <sup>43</sup> were not observed here. At low temperatures, the above mesophases can coexist with the vapor, so that the phase diagram contains not only vapor–liquid but also vapor–stripes, vapor–cylinders, and vapor–clusters coexistence regions, with neighboring regions separated by three-phase domains.

The above-mentioned scenario is obtained both by an analytic implementation of the DFT based on its Landau expansion in powers of the amplitude of the density modulations and by minimization of the full grand potential on purely numerical grounds; however, the two approaches differ appreciably at high density. Specifically, the analytic theory fails to reproduce the strong-segregation regime, where it may even predict unphysical values of the local concentration. Moreover, compared to the numerical results, it strongly underestimates the size of the bcc cluster domain and overestimates that of the stripe domain.

Regardless of its analytic or numerical implementation, according to the mean-field DFT considered here, the width  $\gamma$  of the attractive well, or equivalently, its range  $\xi=(1+\gamma)\sigma$ , is entirely taken into account by incorporating it into the reduced temperature  $T^*$ . Therefore, mixtures corresponding to different values of  $\gamma$  at the same  $T^*$  display the same phase diagram in the  $\rho^*-x$  plane, and the topology of the phase diagram is not affected by  $\gamma$ . For sufficiently wide wells, say  $\gamma \gtrsim 2$ , these predictions are probably realistic, but we expect them to fail for narrow wells such that  $\xi$  is comparable to the hard-sphere diameter  $\sigma$ .

Moreover, the use of the local density approximation (LDA) in the hard-sphere part of the free-energy functional makes it unsuited to describe freezing on an atomic scale. This is the reason why we have refrained from discussing freezing, even though we expect it to be relevant to this study, considering the rather high densities at which the mesophases are predicted to occur. For relatively wide attractions, it might well happen that mesophases similar to those discussed here are found both in the fluid and in the crystal, and that mesophase formation and freezing are, to some extent, independent of each other. This corresponds to the assumption that we made in Ref. 36 in the equimolar case, to draw a tentative phase diagram for  $\gamma = 2$ , including both a stripe fluid and a stripe crystal.

The situation will again be different for short-ranged attractions such that the period of the modulations becomes comparable to particle size. In fact, this is the situation considered in our former simulation study<sup>45</sup> at  $x \neq 0$ . In light of this, it would be interesting to reconsider the phase diagram of the system by a free-energy functional able to describe density modulations at small length scales beyond the LDA. Within the mean-field approximation considered here, a natural way to do so would consist in replacing the LDA

description of the hard-sphere term by that provided by the more accurate weighted-density approximation or fundamental-measure theory.  $^{62-65}$ 

## **ACKNOWLEDGMENTS**

D.P. acknowledges financial support under the National Recovery and Resilience Plan (NRRP), Mission 4, Component 2, Investment 1.1, Call for tender No. 104 published on February 2, 2022, by the Italian Ministry of University and Research (MUR), funded by the European Union—NextGenerationEU—Project Title "Thermal Forces in confined fluids and soft solids"—No. CUP J53D23001310006—Grant Assignment Decree No. 957 adopted on June 30, 2023 by the Italian Ministry of University and Research (MUR).

## **AUTHOR DECLARATIONS**

## **Conflict of Interest**

The authors have no conflicts to disclose.

#### **Author Contributions**

Davide Pini: Funding acquisition (equal); Investigation (equal); Methodology (equal); Software (equal); Writing – original draft (equal). Santi Prestipino: Conceptualization (equal); Investigation (equal); Validation (equal); Writing – review & editing (equal). Dino Costa: Investigation (equal); Visualization (equal); Writing – review & editing (equal). Gianpietro Malescio: Investigation (equal); Visualization (equal); Writing – review & editing (equal). Gianmarco Munaò: Conceptualization (equal); Investigation (equal); Supervision (equal); Writing – review & editing (equal).

#### **DATA AVAILABILITY**

The data that support the findings of this study are available from the corresponding author upon reasonable request.

## APPENDIX: STABILITY OF INHOMOGENEOUS PHASES IN LANDAU THEORY

Here, we derive in some detail the results of the Landau theory for the stability of the inhomogeneous phases presented in Sec. V.

The coefficients C, D, and E of the Landau free energy (45) are given by

$$C = \frac{\rho}{4}\alpha_2 \left[ \frac{\cos^2 \theta}{1+y} + \frac{\sin^2 \theta}{1-y} - \frac{\rho}{2}c_0(\cos \theta + \sin \theta)^2 + \beta_{\lambda}\rho \sin \theta \cos \theta \right], \tag{A1}$$

$$D = -\frac{\rho}{12}\alpha_3 \left[ \frac{\cos^3 \theta}{\left(1 + y\right)^2} + \frac{\sin^3 \theta}{\left(1 - y\right)^2} + \frac{\rho^2}{4} \frac{dc_0}{d\rho} \left(\cos \theta + \sin \theta\right)^3 \right], \quad (A2)$$

$$E = \frac{\rho}{24} \alpha_4 \left[ \frac{\cos^4 \theta}{(1+y)^3} + \frac{\sin^4 \theta}{(1-y)^3} - \frac{\rho^3}{16} \frac{d^2 c_0}{d\rho^2} (\cos \theta + \sin \theta)^4 \right], \quad (A3)$$

with  $\cos \theta$  and  $\sin \theta$  expressed by Eqs. (26a), (26b), and (28).

From the Carnahan–Starling expression (12) of  $c_0$ , we obtain

$$\frac{dc_0}{d\rho} = -6v_0^2 \frac{5 - \eta}{(1 - \eta)^5},\tag{A4}$$

$$\frac{d^2c_0}{d\rho^2} = -24v_0^3 \frac{6-\eta}{(1-\eta)^6}.$$
 (A5)

The quantities  $\alpha_2$ ,  $\alpha_3$ , and  $\alpha_4$  are lattice-dependent constants related to the periodic modulation  $\phi(\mathbf{r})$  introduced in Eq. (37a) by

$$\alpha_n = \frac{1}{v} \int_{\mathcal{C}} d^3 \mathbf{r} \phi^n(\mathbf{r}). \tag{A6}$$

For  $\alpha_2$ , Parseval's identity gives

$$\alpha_2 = \sum_{\mathbf{k}} \hat{\phi}_{\mathbf{k}}^2 = \frac{1}{q},\tag{A7}$$

where Eq. (42) for  $\hat{\phi}_{\mathbf{k}}$  has been taken into account.

For the stripe, cylinder, bcc, and fcc cluster phases considered in Sec. V, the expressions of  $\phi(\mathbf{r})$  and the constants  $\alpha_n$  are *Stripes* 

$$\phi(\mathbf{r}) = \cos(k_0 x),\tag{A8}$$

$$\alpha_2 = \frac{1}{2}, \quad \alpha_3 = 0, \quad \alpha_4 = \frac{3}{8}.$$
 (A9)

Cylinders

$$\phi(\mathbf{r}) = \frac{1}{3} \left[ \cos(k_0 x) + 2 \cos\left(\frac{k_0 x}{2}\right) \cos\left(\frac{\sqrt{3} k_0 y}{2}\right) \right], \quad (A10)$$

$$\alpha_2 = \frac{1}{6}, \quad \alpha_3 = \frac{1}{18}, \quad \alpha_4 = \frac{5}{72}.$$
 (A11)

BCC clusters

$$\phi(\mathbf{r}) = \frac{1}{3} \left[ \cos\left(\frac{k_0 x}{\sqrt{2}}\right) \cos\left(\frac{k_0 y}{\sqrt{2}}\right) + \cos\left(\frac{k_0 x}{\sqrt{2}}\right) \cos\left(\frac{k_0 z}{\sqrt{2}}\right) + \cos\left(\frac{k_0 y}{\sqrt{2}}\right) \cos\left(\frac{k_0 z}{\sqrt{2}}\right) \right], \tag{A12}$$

$$\alpha_2 = \frac{1}{12}, \quad \alpha_3 = \frac{1}{36}, \quad \alpha_4 = \frac{5}{192}.$$
 (A13)

FCC clusters

$$\phi(\mathbf{r}) = \cos\left(\frac{k_0 x}{\sqrt{3}}\right) \cos\left(\frac{k_0 y}{\sqrt{3}}\right) \cos\left(\frac{k_0 z}{\sqrt{3}}\right), \tag{A14}$$

$$\alpha_2 = \frac{1}{8}, \quad \alpha_3 = 0, \quad \alpha_4 = \frac{27}{512}.$$
 (A15)

Equations (A9) and (A15) imply that the coefficient D of the cubic term of Eq. (45) is always zero for the stripe and fcc phases. Moreover, at the equimolar concentration y = 0, Eq. (26) implies  $\cos \theta = \sqrt{2}/2 = -\sin \theta$  so that D vanishes also for the cylinder and bcc phases [see Eq. (A2)]. For D = 0, Eq. (45) describes a second-order

transition that takes place at C=0, i.e., on the  $\lambda$ -surface. Inside the region bounded by the  $\lambda$ -surface, minimization with respect to  $\mathcal A$  for D=0 gives

$$\mathcal{A} = \pm \left(\frac{|C|}{2E}\right)^{1/2},\tag{A16}$$

$$\frac{\Delta(\beta A)}{V} = -\frac{C^2}{4E} = -\frac{\alpha_2^2 C'^2}{\alpha_4 4E'},\tag{A17}$$

where we have introduced the lattice-independent quantities  $C' = C/\alpha_2$ ,  $D' = D/\alpha_3$ , and  $E' = E/\alpha_4$ . From the values of  $\alpha_n$  listed in Eqs. (A9), (A11), (A13), and (A15), we obtain

$$\left(\frac{\alpha_2^2}{\alpha_4}\right)_{\text{stripes}} = \frac{2}{3} > \left(\frac{\alpha_2^2}{\alpha_4}\right)_{\text{cylinders}} = \frac{2}{5} > \left(\frac{\alpha_2^2}{\alpha_4}\right)_{\text{fcc}} = \frac{8}{27} > \left(\frac{\alpha_2^2}{\alpha_4}\right)_{\text{bcc}} = \frac{4}{15}.$$
(A18)

Hence, at equimolar concentration, the stripe phase is always the inhomogeneous phase of the lowest free energy, in agreement with numerical simulation. 35,36 The fcc phase will not be considered in the following because, according to Eq. (A18), its free energy is higher than that of the stripe phase at all concentrations.

At non-equimolar concentration, the coefficient D of the cylinder and bcc phases is non-vanishing, thereby making the transition from the homogeneous to the inhomogeneous fluid first-order: before reaching the  $\lambda$ -surface at C=0, for  $C=D^2/4E$ , the order parameter  $\mathcal A$  jumps discontinuously from  $\mathcal A=0$  to  $\mathcal A=-D/(2E)$ . In terms of the lattice-independent quantities C', D', and E', the transition takes place at

$$C' = \zeta \frac{D'^2}{4F'},\tag{A19}$$

where  $\zeta$  is the lattice-dependent constant given by

$$\zeta = \frac{\alpha_3^2}{\alpha_2 \alpha_4},\tag{A20}$$

with

$$\zeta_{\rm bcc} = \frac{16}{45} > \zeta_{\rm cylinders} = \frac{4}{15},\tag{A21}$$

showing that the transition from the homogeneous fluid to the bcc cluster phase preempts that from the homogeneous fluid to the cylinder phase.

Inside the inhomogeneous region, minimization of Eq. (45) for  $D \neq 0$  gives

$$A = \frac{-3D \pm (9D^2 - 32CE)^{1/2}}{8E},$$
 (A22)

where the plus sign holds for D < 0 and the minus sign for D > 0. In both cases, by inserting Eq. (A22) into Eq. (45), we obtain

$$\frac{\Delta(\beta A)}{V} = \frac{C^{\prime 2} f(z)}{6E^{\prime} z^2},\tag{A23}$$

where z is the lattice-independent variable defined as

$$z = -\frac{4C'E'}{D'^2},$$
 (A24)

and the function f(z) is given by

$$f(z) = -\delta \left[ 27 + \frac{36}{\zeta} z + \frac{8}{\zeta^2} z^2 + \left( 9 + \frac{8}{\zeta} z \right)^{3/2} \right]. \tag{A25}$$

The lattice-dependent constant  $\delta$  is expressed as

$$\delta = \frac{3}{16} \frac{\alpha_3^4}{\alpha^3},\tag{A26}$$

with

$$\delta_{\text{bcc}} = \frac{64}{10125} > \delta_{\text{cylinders}} = \frac{2}{375}.$$
 (A27)

For the stripe phase, for which  $\alpha_3 = 0$ , both  $\zeta$  and  $\delta$  vanish. In this limit, Eq. (A25) gives  $f(z) = -z^2$  which, when substituted into Eq. (A23), gives back the free energy of the stripes.

Figure 14 displays f(z) for the stripe, cylinder, and bcc cluster phases for  $z > -\zeta$ , which corresponds to the inhomogeneous domain. The bcc phase is that of lowest free energy for z < 0.22, whereas the cylinder phase prevails for 0.22 < z < 8.61, and the stripe phase for z > 8.61.

At fixed density and temperature, z decreases as the concentration x moves from x = 0.5 to higher or smaller values. Therefore, if

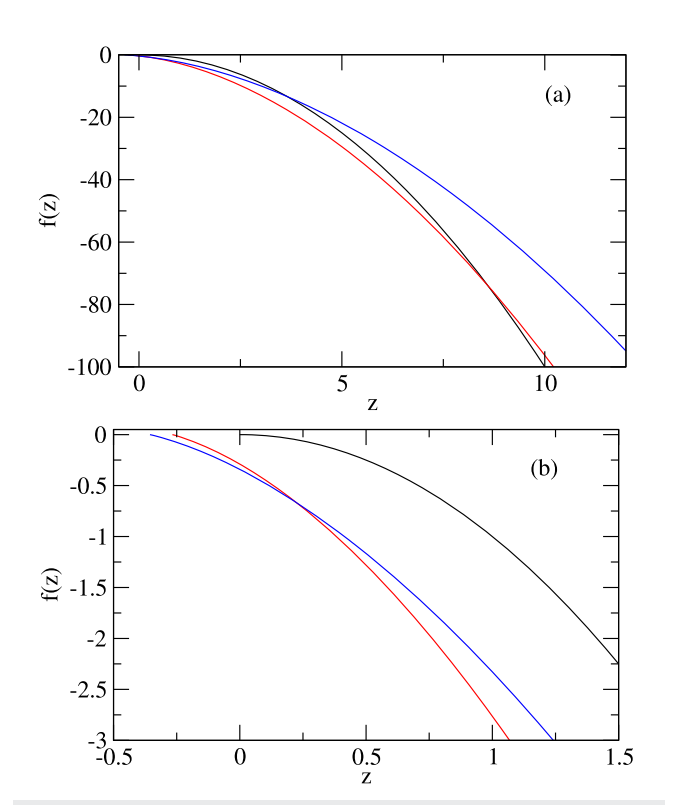


**FIG. 14.** Function f(z) defined in Eq. (A25) for the cluster, cylinder, and stripe phases at large z [panel (a)] and small z [panel (b)]. Black line: stripes. Red line: cylinders. Blue line: clusters. At each z, the most stable phase is that with the lowest f(z) [see Eq. (A23)].

one starts from the equimolar mixture inside the inhomogeneous region and departs from equimolarity, one sweeps the sequence stripes-cylinders-bcc clusters-homogeneous fluid.

#### REFERENCES

- <sup>1</sup>Z. Zhang, M. A. Horsch, M. H. Lamm, and S. C. Glotzer, Nano Lett. 3, 1341 (2003).
- <sup>2</sup>S. Sacanna, M. Korpics, K. Rodriguez, L. Colón-Meléndez, S. H. Kim, D. J. Pine, and G.-R. Yi, Nat. Commun. 4, 1688 (2013).
- <sup>3</sup>S. C. Glotzer and M. J. Solomon, Nat. Mater. **6**, 557 (2007).
- <sup>4</sup>D. J. Kraft, R. Ni, F. Smallenburg, M. Hermes, K. Yoon, D. A. Weitz, A. van Blaaderen, J. Groenewold, M. Dijkstra, and W. K. Kegel, Proc. Natl. Acad. Sci. U. S. A. **109**, 10787 (2012).
- <sup>5</sup>P. Prinsen, P. B. Warren, and M. A. J. Michels, Phys. Rev. Lett. 89, 148302 (2002).
   <sup>6</sup>D. Pini, Soft Matter 14, 6595 (2018).
- <sup>7</sup>B. Yu, B. Li, P. Sun, T. Chen, Q. Jin, D. Ding, and A.-C. Shi, J. Chem. Phys. 123,
- <sup>8</sup>H.-J. Qian, Z.-Y. Lu, L.-J. Chen, Z.-S. Li, and C.-C. Sun, Macromolecules 38, 1395–1401 (2005).
- <sup>9</sup> A. Kumar and V. Molinero, J. Phys. Chem. Lett. **8**, 5053 (2017).
- <sup>10</sup>B. A. Lindquist, S. Dutta, R. B. Jadrich, D. J. Milliron, and T. M. Truskett, Soft Matter 13, 1335 (2017).
- <sup>11</sup>S. Jury, P. Bladon, M. Cates, S. Krishna, M. Hagen, N. Ruddock, and P. Warren, Phys. Chem. Chem. Phys. 1, 2051 (1999).
- <sup>12</sup>P. I. O'Toole, G. Munaò, A. Giacometti, and T. Hudson, Soft Matter 13, 7141 (2017).
- <sup>13</sup> A. J. Archer, D. Pini, R. Evans, and L. Reatto, J. Chem. Phys. **126**, 014104 (2007).
- <sup>14</sup>J. C. F. Toledano, F. Sciortino, and E. Zaccarelli, Soft Matter 5, 2390 (2009).
- <sup>15</sup>H. J. Zhao, V. R. Misko, and F. M. Peeters, New J. Phys. **14**, 063032 (2012).
- <sup>16</sup>P. D. Godfrin, N. E. Valadez-Perez, R. Castañeda-Priego, N. Wagner, and Y. Liu, Soft Matter 10, 5061 (2014).
- <sup>17</sup>Y. Zhuang and P. Charbonneau, J. Phys. Chem. B **120**, 7775 (2016).
- <sup>18</sup>Y. Zhuang and P. Charbonneau, J. Phys. Chem. B **120**, 6178 (2016).
- <sup>19</sup>Y. Zhuang, K. Zhang, and P. Charbonneau, Phys. Rev. Lett. 116, 098301 (2016).
- <sup>20</sup>D. Costa, G. Munaò, J. M. Bomont, G. Malescio, A. Palatella, and S. Prestipino, Phys. Rev. E **108**, 034602 (2023).
- <sup>21</sup>G. Malescio and G. Pellicane, Nat. Mater. 2, 97 (2003).
- <sup>22</sup>G. Malescio and G. Pellicane, Phys. Rev. E 70, 021202 (2004).
- <sup>23</sup> M. A. Glaser, G. M. Grason, R. D. Kamien, A. Košmrlj, C. D. Santangelo, and P. Ziherl, Europhys. Lett. **78**, 46004 (2007).
- <sup>24</sup>G. J. Pauschenwein and G. Kahl, J. Chem. Phys. 129, 174107 (2008).
- <sup>25</sup>G. J. Pauschenwein and G. Kahl, Soft Matter 4, 1396 (2008).
- <sup>26</sup>J. Fornleitner and G. Kahl, Europhys. Lett. **82**, 18001 (2008).
- <sup>27</sup> J. Fornleitner and G. Kahl, J. Phys.: Condens. Matter 22, 104118 (2010).
- <sup>28</sup>O. Patsahan, M. Litniewski, and A. Ciach, Soft Matter 17, 2883 (2021).
- <sup>29</sup> A. Ciach, A. D. Virgiliis, A. Meyra, and M. Litniewski, Molecules 28, 1366 (2023).
- 30 O. Patsahan, A. Meyra, and A. Ciach, Soft Matter 20, 1410 (2024).
- <sup>31</sup> A. De Virgiliis, A. Meyra, and A. Ciach, Molecules **29**, 1512 (2024).
- <sup>32</sup> M. Litniewski, W. T. Gozdz, and A. Ciach, Soft Matter 21, 6801 (2025).
- <sup>33</sup>C. I. Mendoza and E. Batta, Europhys. Lett. **85**, 56004 (2009).
- <sup>34</sup>L. A. Padilla, A. A. León-Islas, J. Funkhouser, J. C. Armas-Pèrez, and A. Ramìrez-Hernández, J. Chem. Phys. 155, 214901 (2021).
- <sup>35</sup>G. Munaò, D. Costa, G. Malescio, J. M. Bomont, and S. Prestipino, Phys. Chem. Chem. Phys. 25, 16227 (2023).
- <sup>36</sup>S. Prestipino, D. Pini, D. Costa, G. Malescio, and G. Munaò, J. Chem. Phys. 159, 204902 (2023).

- <sup>37</sup> J. Hou, M. Li, and Y. Song, Nano Today **22**, 132 (2018).
- <sup>38</sup>S. Watanabe, K. Inukai, S. Mizuta, and M. T. Miyahara, Langmuir **25**, 7287 (2009).
- <sup>39</sup>Y. Mino, S. Watanabe, and M. T. Miyahara, ACS Appl. Mater. Interfaces 4, 3184 (2012).
- <sup>40</sup>C. E. Caicedo-Carvajal and T. Shinbrot, Dev. Biol. 315, 397 (2008).
- <sup>41</sup>T. Shinbrot, Y. Chun, C. Caicedo-Carvajal, and R. Foty, Biophys. J. **97**, 958 (2009)
- <sup>42</sup> A. J. Archer, C. N. Likos, and R. Evans, J. Phys.: Condens. Matter 16, L297 (2004).
- 43 D. Pini, A. Parola, and L. Reatto, J. Chem. Phys. 143, 034902 (2015).
- <sup>44</sup>D. Pini and A. Parola, Soft Matter **13**, 9259 (2017).
- <sup>45</sup>S. Prestipino, D. Pini, D. Costa, G. Malescio, and G. Munaò, Phys. Rev. E 112, 025413 (2025).
- <sup>46</sup>J. G. Kirkwood, in *Phase Transformations in Solids*, edited by R. Smoluchowski, J. E. Mayer, and W. A. Weyl (John Wiley & Sons, Inc., New York, 1951), p. 67.
- <sup>47</sup>A. Ciach, Mol. Phys. **109**, 1101 (2011).
- <sup>48</sup> J. P. Hansen and I. R. McDonald, *Theory of Simple Liquids*, 3rd ed. (Academic Press, New York, 2006).

- <sup>49</sup> A. Parola and L. Reatto, Phys. Rev. A 44, 6600 (1991).
- $^{\bf 50}$  N. B. Wilding, F. Schmid, and P. Nielaba, Phys. Rev. E **58**, 2201 (1998).
- <sup>51</sup> D. Pini, M. Tau, A. Parola, and L. Reatto, Phys. Rev. E **67**, 046116 (2003).
- <sup>52</sup> A. Mkanya, G. Pellicane, D. Pini, and C. Caccamo, J. Phys.: Condens. Matter 29, 365102 (2017).
- <sup>53</sup> A. Ciach, Phys. Rev. E 78, 061505 (2008).
- <sup>54</sup> A. Ciach and W. T. Góźdź, Condens. Matter Phys. **13**, 23603 (2010).
- <sup>55</sup>A. J. Archer, C. Ionescu, D. Pini, and L. Reatto, J. Phys.: Condens. Matter 20, 415106 (2008).
- <sup>56</sup>S. A. Brazovskii, Sov. Phys. JETP **41**, 85 (1975).
- <sup>57</sup> A. Ciach, Soft Matter **14**, 5497 (2018).
- <sup>58</sup>K. Momma and F. Izumi, J. Appl. Crystallogr. **44**, 1272 (2011).
- <sup>59</sup>D. A. Huse and S. Leibler, J. Phys. **49**, 605 (1988).
- 60 M. G. Noro and D. Frenkel, J. Chem. Phys. 113, 2941 (2000).
- <sup>61</sup> J. Largo, M. A. Miller, and F. Sciortino, J. Chem. Phys. **128**, 134513 (2008).
- <sup>62</sup>P. Tarazona, Phys. Rev. A **31**, 2672 (1985).
- <sup>63</sup> P. Tarazona, Phys. Rev. A **32**, 3148 (1985).
- 64 A. R. Denton and N. W. Ashcroft, Phys. Rev. A 39, 4701 (1989).
- 65 Y. Rosenfeld, Phys. Rev. Lett. 63, 980 (1989).